LBL-32433
UC-413
Preprint

Lawrence Berkeley Laboratory
UNIVERSITY OF CALIFORNIA

Submitted to Nuclear Physics A

Complex Fragment Production and Multifragmentation in ^{139}La-induced Reactions at 35, 40, 45 and 55 MeV/u

P. Roussel-Chomaz, N. Colonna, Y. Blumenfeld, B. Libby,
G.F. Peaslee, D.N. Delis, K. Hanold, M.A. McMahan,
J.C. Meng, Q.C. Sui, G.J. Wozniak, and L.G. Moretto

May 1992

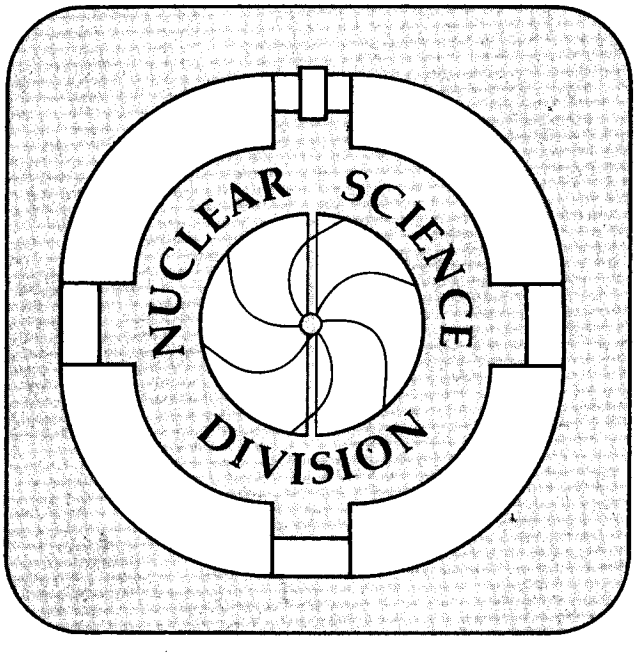

Prepared for the U.S. Department of Energy under Contract Number DE-AC03-76SF00098

DISCLAIMER

Complex Fragment Production and Multifragmentation in ^{139}La-induced Reactions at 35, 40, 45 and 55 MeV/u

P. Roussel-Chomaz[1], N. Colonna, Y. Blumenfeld[2], B. Libby[3], G.F. Peaslee[4], D.N. Delis, K. Hanold, M.A. McMahan, J.C. Meng[5], Q.C. Sui[5], G.J. Wozniak and L.G. Moretto

Nuclear Science Division, Lawrence Berkeley Laboratory, Berkeley, California 94720

H. Madani, A.A. Marchetti and A.C. Mignerey

Department of Chemistry, University of Maryland, College Park, Maryland 20742

G. Guarino

Instituto Nazionale di Fisica Nucleare (INFN), Sezione di Bari, Bari 70126, Italy

N. Santoruvo and I. Iori

Università di Milano, Milano 20133, Italy

S. Bradley

Kaman Sciences, 2560 Huntington Av., Alexandria, VA 22303

Abstract: Complex fragment emission (Z > 3) has been studied in the reactions of 35, 40, 45 and 55 MeV/u ^{139}La + X. Charge, angle, and energy distributions were measured inclusively and in coincidence with other complex fragments, and were used to extract source rapidities, velocity distributions, and cross sections. Multifragment events increase with both bombarding energy and entrance-channel mass asymmetry. The excitation functions for multifragment events rise strongly with excitation energy. These excitation funcions are independent of the target-projectile combination and bombarding energy suggesting the formation fo an intermediate nuclear system, whose decay properties depend mainly on its excitation energy and angular momentum.

NUCLEAR REACTIONS: ^{12}C, ^{27}Al, ^{40}Ca, ^{nat}Cu, ^{139}La (^{139}La, X), E = 35, 40, 45, 55 MeV/nucleon; measured σ(fragment E,θ), deduced source velocities, charge distributions; measured (fragment)(fragment-coin).

---

1) On leave from the SEPN, Centre D'Etudes Nucleaires Saclay, 91191 Gif-sur-Yvette, Cedex, France
2) On leave from the Institut de Physique Nucleaire, 91406 Orsay, Cedex, France
3) Present address: University of Maryland, College Park, MD 20247
4) Present address: Cyclotron Laboratory, Michigan State University, East Lansing, MI 48824
5) On leave from the Institute of Atomic Energy, Beijing, China

1-Introduction

Complex-fragment emission is now a well established mode of decay for a compound nucleus [1]. While it is quite rare at low excitation energy, due to the associated high barrier (typically 20 to 40 MeV) [2-4], it becomes relatively abundant at high excitation energies and angular momenta [5-13]. Furthermore, its distinctive features have been used to characterize hot compound nuclei formed in both low- and intermediate-energy heavy ion reactions [8-13].

Compound nuclei are formed in complete fusion reactions at low bombarding energies. As the bombarding energy increases, incomplete fusion sets in. Still, the product of the incomplete fusion can relax into a hot compound nucleus, which can be characterized in terms of its mass, excitation energy and, to a lesser extent, angular momentum, by detecting in coincidence the two fragments arising from its binary decay. Studies of this kind are particularly easy to make in reverse kinematics. For very mass-asymmetric entrance channels, the velocity distribution of the sources of binary complex-fragment emission is very sharply peaked. It corresponds to complete fusion at low bombarding energies [4,9,10,12], and it progresses to values characteristic of incomplete fusion at higher bombarding energies [8,13]. The sharpness of the source velocity distributions for these very asymmetric systems has been of key importance in the unraveling of the reaction mechanism [1].

For more symmetric entrance channels, the situation is more complex. For instance, in the reaction $^{139}La + ^{58}Ni$ at 18 MeV/u, the source velocity distribution determined from binary coincidences is very broad [14]. In it one can distinguish a rather broad peak, corresponding to complete fusion, and a leading edge covering the velocity range corresponding to the entire range of mass transfers. This experiment demonstrated the usefulness of the reverse kinematics technique, which allows one to characterize kinematically the process of incomplete fusion on the one hand, and its fusion product on the other. This technique permits selection of the excitation energy by setting a window on the source velocity. In the incomplete fusion picture, a given source velocity corresponds to a

given mass transfer and that mass transfer corresponds to a given excitation energy, and, to a somewhat more uncertain degree, to a given angular momentum. Thus, at a fixed bombarding energy, we can "dial", as it were, the excitation energy of the fused product, and obtain an entire excitation function. In reality, preequilibrium emission creates some complications, as will be discussed in a later section. This technique makes it possible to extend the study of the incomplete fusion process along the two relevant "coordinates": the bombarding energy, and the entrance-channel-mass-asymmetry.

In the experiments mentioned above, reference was made to "binary" decays, in the sense that the product of complete or incomplete fusion underwent binary decay. Of course, in the case of incomplete fusion these processes were at least ternary, accompanied, as they were, by the incomplete-fusion spectator.

With increasing bombarding energy, however, one encounters multifragment events that cannot be reduced to this "trivial" case [15-21]. Thus, the question arises as to the origin of these multifragment events. Is it possible to characterize a source of multifragment events in terms of its mass, charge, excitation energy, and angular momentum, similarly to what was done for "binary" decays? In principle it is, and in fact the very same kinematic reconstruction used for "binary" events can be generalized to events with any number of fragments. If this kinematic reconstruction works, one can obtain, at any given bombarding energy, the relative excitation functions of binary, ternary, quaternary etc., events. These excitation functions could be the key to unraveling the physical process responsible for multifragment production.

In order to achieve some of the goals illustrated above, we have investigated the sources of binary, ternary, quaternary etc., events in a series of ^{139}La-induced reactions. The entrance-channel mass-asymmetry coordinate and its role in incomplete fusion was investigated by means of the following reactions: ^{139}La + ^{12}C, ^{27}Al, ^{40}Ca, ^{51}V, ^{nat}Cu and ^{139}La. The bombarding energy dimension was explored by choosing the bombarding energies 35, 40, 45 and 55 MeV/u. By means of these and similar, although somewhat less sophisticated studies at lower bombarding energies, we have obtained a very comprehensive

coverage that may throw light on these intriguing and complex processes. The experimental method is detailed in Section 2. Section 3 presents the results obtained from the inclusive data. Coincidence measurements are discussed in Section 4. Finally the conclusions are presented in Section 5. A portion of this work has been published previously [18]. Extensive simulations of these systems are being carried with a BNV code and are described in separate papers [22, 23].

2-Experimental Procedure

The experiments were performed at the Lawrence Berkeley Laboratory Bevalac. Beams of ^{139}La ions impinged on targets of ^{12}C, ^{27}Al, ^{40}Ca and ^{51}V at 35 MeV/u; ^{12}C, ^{27}Al, ^{40}Ca, ^{51}V, and ^{nat}Cu at 40 MeV/u; and ^{27}Al, ^{51}V, ^{nat}Cu and ^{139}La at 45 and 55 MeV/u. The thickness of all of the targets was chosen to be approximately 2 mg/cm^2.

The reaction products were detected in two arrays of 3x3 Si-Si(Li)-plastic telescopes [24]. The detection system is schematically illustrated in fig. 1. The two arrays were centered at 15^o on each side of the beam axis, and had an acceptance of 21^o in the horizontal and vertical planes. Each telescope had an active area of 4.5x4.5 cm^2, and its total area was 5.5x5.7 cm^2. A gold foil (3 mg/cm^2 thick) was placed in front of each telescope for electron suppression.

Each telescope consisted of three elements: a 300-μm thick Si ΔE detector, a 5-mm thick position-sensitive Si(Li) E detector, and a 7.6-cm thick plastic scintillator with its photomultiplier tube, used as an E detector for the charged particles that punched through the first two elements of the telescope. The fragment positions were determined by resistive division across one face of the Si detectors. Each Si detector had fifteen 3-mm wide discrete strips[25]. In each telescope, the strips of the two Si detectors were arranged orthogonally to give both the in- and out-of-plane positions of the detected fragment.

The energy calibrations were performed by directly exposing the detectors to low intensity "cocktail" beams[26], composed of ions with the same mass-to-charge ratio

(namely $^{14}N^{4+}$, $^{28}Si^{8+}$, $^{56}Fe^{16+}$, and $^{84}Kr^{24+}$). The calibrations were repeated at several bombarding energies. Fig. 2 presents a typical spectrum obtained with one of the multiple calibration beams. The ^{139}La beam itself was used to provide an additional calibration point. The different charges and energies of the calibration beams allowed for a direct estimate of the pulse height defect, using a method similar to that described in ref. [27]. A correction for the energy loss in the target and in the Au foils was also performed. The energy resolution achieved with this procedure is about 1.5%. The charge resolution obtained from the ΔE-E measurement allowed for Z identification up to Z = 57. Fig. 3 shows a representative Z spectrum, in both linear and logarithmic scales.

Only fragments with Z > 3 were considered in this analysis. The mass corresponding to a given charge was estimated using the expression [8]:

$$A = 2.08\,Z + 0.0029\,Z^2. \qquad (1)$$

In order to measure absolute cross sections, the beam charge was collected in a Faraday cup and integrated. The Faraday cup was calibrated with a current source and by measuring the Rutherford scattering of ^{139}La from a ^{197}Au target at all bombarding energies.

3-Inclusive Data

3-1 Velocity diagrams

Preliminary information on the reaction mechanism and the emission process can be obtained by plotting, for a given Z-value, the cross section $d^2\sigma/ dv_{\|}dv_{\perp}$ in velocity space. Sharp circles in velocity space - usually referred to as Coulomb circles because of their origin - are produced by the binary decay of a highly equilibrated source moving with a well-defined velocity [8]. At low bombarding energies, these Coulomb circles are centered at the complete-fusion velocity. At higher energies, where incomplete fusion sets in, the circles become smeared out, as a consequence of the continuous range of velocities and sizes of the sources produced in the incomplete fusion process [14]. Similarly, the circles are expected to be smeared out as soon as multifragment emission becomes important, since in such events

the emission velocities of the fragments in the source frame are not as well defined as in the case of binary decay. For both of the above reasons, we expected a smeared out pattern in the 40 - 55 MeV/u region.

To illustrate the role of the entrance-channel mass asymmetry and of the incident energy, some representative examples of the invariant cross section in the $v_{\parallel}$ - $v_{\perp}$ plane are presented for the systems $^{139}La + ^{12}C$ at 40 MeV/u (fig. 4), $^{139}La + ^{27}Al$ (figs. 5&6) and $^{139}La + ^{nat}Cu$ at 40 and 55 MeV/u (figs. 7&8). In the case of the ^{12}C target, Coulomb rings can be observed up to Z=25, but they are considerably broadened. Two effects contribute to this broadening. The range of source velocities associated with the continuum of incomplete fusion processes produces a smearing along the $v_{\parallel}$ axis, whereas the sequential evaporation of light charged particles from the fragments broadens the distribution in all directions. For the ^{27}Al target at 40 and 55 MeV/u, we observe a further broadening probably due to non-binary processes and the Coulomb rings can barely be distinguished for $5<Z<20$. This effect is even more pronounced for the heavier ^{nat}Cu target, where disk-shaped patterns are observed. For the heavier fragments, the distributions show very little dependence on the incident beam energy and the entrance-channel-mass-asymmetry. In all cases, disk-like distributions are observed. In this intermediate-energy regime, incomplete fusion, extensive particle evaporation, and multifragment emission, wash out the simple Coulomb circles observed at lower bombarding energy.

The Coulomb circles are not sufficiently well defined to determine the source velocity from the singles in a straightforward way. Therefore, we have determined the source velocity from the coincidence data. In the present analysis, for the coincidence events, the source velocity was given by the following expression:

$$\mathbf{V}_S = \Sigma m_i \mathbf{V}_i / \Sigma m_i \qquad (2)$$

where m_i and $\mathbf{V}_i$ are the mass and the velocity in the laboratory frame of the i-th fragment, and the summation is carried out over all the detected fragments. In fig. 9, the extracted source velocities are presented for all targets and energies. At all bombarding energies, the

source velocity is roughly independent of the fragment mass. There is a small target dependence, with the lighter targets giving rise to somewhat larger source velocities. Therefore, for each system a unique "average" value of the source velocity was assumed in the extraction of the emission velocity from the singles data.

In fig. 10 the average-emission velocity, defined as $\langle V_e \rangle = \langle |V_{lab} - V_S| \rangle$, is plotted as function of the charge of the detected fragment. For all the studied systems, the emission velocities are very similar to each other. Keeping in mind the Coulomb origin of the emission velocity, this similarity indicates that, on the average, the mass of the decaying system does not depend strongly on the target, or on the incident energy.

3-2 Angular distributions

The experimental angular distributions may provide information on the relative importance of equilibrium and non-equilibrium emission processes [9]. Some representative examples of the measured angular distributions are shown in figs. 11-13 for the different targets and three bombarding energies. These angular distributions are plotted in a frame moving with the average source velocity, as determined from eq. (2).

The first striking feature of the angular distributions is their similar evolution as a function of the fragment charge for the different systems and the different energies. The angular distributions are backward peaked for $Z < 18$, forward peaked for $Z > 22$ and roughly flat in the region in between. This lack of Z-values with isotropic angular distributions is in contrast to the pattern at lower bombarding energy, where isotropic distributions are observed for a large range of Z-values between the target and the projectile. At low bombarding energies, the anisotropic distributions near the projectile and target Z-values are due to quasi-elastic and deep-inelastic components [12] superimposed on the compound nucleus component. At 35 - 55 MeV/u, the pervasive presence of anisotropic angular distributions for nearly all Z-values, suggests the presence of additional non-equilibrium emission processes. These results extend a previous study of the 50 MeV/u $^{139}La + ^{12}C$

reaction which, for a limited range of masses and over a limited angular range, observed forward-backward ratios consistent with isotropy[28].

3-3 Cross Sections

The angular distributions shown in figs. 11-13, were fit (solid lines) and the results of the fits were used to estimate the integrated cross sections.

The extracted cross sections are shown in figs. 14-16 as a function of the detected Z value. In all cases, the statistical error bars are smaller than the size of the data points. The error bars shown are associated with the extraction procedure and with the absolute normalization. Due to the reduced angular coverage, a larger uncertainty is present for the largest Z-values. To estimate these systematic errors, the angular distributions were fit with two different procedures: a quadratic fit and a fit employing a linear plus exponential functional form, similar to the one used in ref [12]. The error bar indicates the difference in the integrated cross sections obtained with these two procedures.

The charge distributions for the systems $^{139}La + ^{12}C$ and ^{27}Al at 18 MeV/u [12] are consistent with statistical emission from a system above the Businaro-Gallone point [29], with a maximum yield at symmetry ($Z \approx 31$-33), due to the corresponding minimum in the potential energy. In contrast, all the charge distributions measured for these systems between 40 and 55 MeV/u are either U-shaped or decrease monotonically over the entire measured Z-range, with a flattening at large Z values in some cases. The overall flattening of the charge distributions could be explained by the increase of the nuclear temperature with increasing incident energy, which tends to make all decay channels more equally probable. On the other hand, the overall decrease with Z-value could be associated with multifragmentation. In the presence of multibody breakup, the yields for the lighter fragments are expected to increase. At the same time, a corresponding depletion in the region of medium and heavy fragments is produced, since fewer of them survive as a consequence of the breaking of the system in several fragments. This trend is particularly visible in the case of

the 55 MeV/u $^{139}La + ^{nat}Cu$ reaction. Due to the large available center of mass energy, in particular for the more symmetric entrance channels, multifragmentation is likely to play an important role in the complex fragment production in the energy range considered in this experiment.

4-Coincidence Data

4-1 Twofold events

A global overview of the reaction can be obtained by examining the two-fold complex fragment coincidence data. The source velocity was reconstructed on an event-by-event basis from the velocities and the masses of the detected fragments, by means of the eq. (2). In Figs. 17-18, contour plots in the plane of the source velocity (normalized to the beam velocity) and the total detected charge are present for 2-fold events at seven different bombarding energies and four entrance-channel-mass-asymmetries. The data corresponding to ^{129}Xe beams, which have been obtained in a different experiment [28], have been shifted by 3 charge units to facilitate the comparison ($\Delta Z_{La-Xe} = 3$). The 18 MeV/u data [12,14] represent a low energy benchmark, since at this energy the reaction mechanisms are better understood. The horizontal lines indicate the complete fusion velocity for each system, and the vertical arrows the projectile charge. It should be noted that the detection system used in the experiments at 18, 26 and 31 MeV/u was different than that used at higher energies and that the differences in detection acceptances could bias the comparison. However, as a test, the data obtained at 55 MeV/u, were filtered through the horizontal central row of both detector arrays used in the present studies, to simulate the low energy experiment's detection acceptance. After filtering, the observed patterns did not change significantly.

In these figures, the first column corresponds to the most asymmetric system $^{139}La/^{129}Xe + ^{12}C$. This system, which has relatively low available energies in the center of mass, presents a very simple pattern. At 18 MeV/u, the source velocity distribution peaks at the value expected for complete fusion, which corresponds to the solid line, and the total

charge detected is equal to the total charge of the system ($Z_P + Z_T = 63$). In this case, complete fusion has occurred and primarily neutrons have been evaporated. When the incident energy increases, the distributions move towards a higher source velocity and a lower total detected charge. The higher velocity corresponds to the onset of incomplete fusion, since, in reverse kinematics, when the projectile picks up less mass from the target, it is slowed down to a lesser degree. A similar description applies to the somewhat heavier ^{27}Al target. The only difference is that, due to the higher excitation energies, the evaporation is more extensive, and the detected charge is smaller than that of the primary compound nucleus ($Z_P + Z_T = 70$), even at 18 MeV/u.

The pattern observed for the heavier targets ^{48}Ti,^{64}Ni/^{nat}Cu is more complicated. At 18 MeV/u we observe events ranging from complete fusion to incomplete fusion. The figures show a ridge going to lower total charge as the source velocity increases. This pattern is expected when a range of incomplete fusion processes are present.

As the incident energy and the excitation energy available in the reaction increase, the pattern shifts towards lower Z values and rotates because of the secondary evaporation process. The competing role of incomplete fusion and charged particle evaporation is illustrated schematically in fig. 19. The thick line represents the range of primary products, from the incomplete fusion process, prior to evaporation (this should be approximately the same at all bombarding energies). The dashed lines to the left show the total charge after evaporation as the bombarding energy (excitation energy) is increased. Since the maximum excitation energy is always for complete fusion, the dashed line should rotate towards the left as the bombarding energy is increased. A vertical line means that all of the charge gained in the incomplete fusion process is equal to the charge lost by evaporation. This is roughly the case for the 31 MeV/u reactions. Above this energy, for each charge unit transferred from the target to the projectile, more than one charge unit is lost on the average by evaporation.

The correlation between the measured charges of the two fragments is also instructive, since it allows one to determine whether the decay mechanism is predominantly binary or

multibody. If the final state is binary, the contour plots should be dominated by a band of events peaking at $Z_1+Z_2 \approx Z_{source}$. If the exit channel is actually multibody with one or several fragments not detected, the events should fall below the line.

The measured Z_1 - Z_2 correlations for the systems studied are shown in figs. 20-21. The pattern observed for the La/Xe + C reactions is very clear. For this very asymmetric system, the contour plots show a distinct band with a total charge close to the sum of the projectile and target Z values, thus illustrating the binary nature of the process. The band broadens and shifts towards smaller total charge as the incident energy increases, because of evaporation. In the case of the ^{27}Al target, this effect becomes more important, and, at the highest incident energy, the scattering of events indicates that for a large fraction of the "binary" events are in fact multibody events where only two of the fragments have been detected. This pattern is even more pronounced for the heavier targets, where the two-body band disappears completely by 35 MeV/u. These two figures illustrate the dramatic changes observed in the data between 18 and 55 MeV/u, as the reaction evolves from primarily two-body to multi-body.

4-2 N-fold events

We define n-fold events, as events with more than two $Z \geq 4$ fragments detected in coincidence.

Figs. 22-24 show the total Z distributions for n-fold events for all the systems studied at 40, 45 and 55 MeV/u. At 40 MeV/u, for the ^{12}C target, a narrow peak is observed for the 2-fold events in the Z_{total} spectrum. As the mass of the target is increased, this peak broadens and shifts to lower detected charge with an increasing low Z tail. These effects arise from the larger range of mass transfers and from the increase of light particle evaporation due to the larger range of available excitation energies. The tail at low total detected charge observed for the two-fold events is associated with higher n-fold events where only two fragments are detected. The same Z_{total} distributions for 3-fold and 4-fold events presents a peak centered

at approximately the same value, but with a reduced tail, indicating that most of these events are complete.

At 45 MeV/u broad peaks are observed in the 2-fold spectra for the lighter ^{27}Al and ^{51}V targets with an extensive low Z tail. For the heavier ^{nat}Cu and ^{139}La targets, very broad distributions are observed. [The peak near Z = 52 in the ^{139}La target spectrum is due to a ^{16}O impurity in the target.] For the 3- and 4-fold events, the tails are reduced and, for the heavier targets, the distributions sharpen up and move to larger values of Z_{total} which is consistent with a larger fraction of the total charge being detected.

At 55 MeV/u a peak is only observed for the ^{27}Al target in the 2-fold spectrum. For the heavier targets, no peaks are observed and the distribution montonically decreases with increasing Z_{total}. For the 4-fold fold events, a broad peak is observed, whose position decreases with increasing target mass.

In what follows, only events with total measured charge larger than 30 will be considered, in order to keep the contamination arising from incompletely detected events to a reasonable level, and to avoid biasing the kinematic reconstruction of the event.

The normalized source velocity distributions obtained at 40, 45 and 55 MeV/u for all the targets and the different fragment multiplicities are presented in figs. 25-27. The observed peaks broaden significantly as the mass of the target is increased. In the framework of the incomplete fusion model, the increased width can be explained by a broader range of impact parameters giving rise to a larger range of incomplete fusion products. Light particle evaporation also contributes to the broadening of the source velocity distribution. This last contribution has been estimated at 40 MeV/u [18] with the statistical code GEMINI [9]. In the case of the ^{12}C target, the width can be explained almost entirely by light particle evaporation, whereas, for the heavier targets, evaporation accounts only for a third to a half, at most, of the observed width. Therefore, for these heavy targets, the width of the source velocity distribution can effectively be associated with a range of incomplete fusion processes.

At each energy, for a given target, the requirement of a larger multiplicity of complex fragments selects out events with lower source velocities, which, in an incomplete fusion picture, correspond to higher excitation energies. A similar result has also been reported in the case of the Ne + Au reaction at 60 MeV/u by comparing the two and three-body events [15].

4.3 Dalitz plots

Dalitz plots have been used to investigate the three-body decays. In this plot, each three-fold event is represented by a point in a triangle, so that the distances to the sides of the triangle correspond to the values Z_1/Z_{tot}, Z_2/Z_{tot}, Z_3/Z_{tot}. Therefore, an event with three equally-sized fragments is represented as a point in the center of the triangle, while an event with one large fragment and two small ones is located in one of the corners. Finally an event with two medium sized fragments and a small one is located in the middle of one side of the triangle. The Dalitz plots presented in fig. 28, have been symmetrized by randomly assigning Z_1, Z_2, Z_3. A gate has also been applied to the total detected charge ($Z_{tot}>30$). The data at 45 MeV/u are not reported on this figure, due to the lower statistics at this energy.

For the system with the lowest available energy in the center of mass, the lightest target (^{27}Al), and the lowest bombarding energy (35 MeV/u), only the vertices of the triangle are populated. This indicates that at low excitation energies, the excited nuclear system undergoing 3-body decay strongly prefers to decay into one heavy and two light fragments. As the excitation energy increases (as for the ^{27}Al target at 55 MeV/u and the heavier targets at 35 and 40 MeV/u), the perimeter is also populated in addition to the vertices, leaving a depression in the center of the triangle. For the highest excitation energy (the ^{nat}Cu target at 55 MeV/u), the center of the triangle becomes populated. However, the vertices and sides of the triangle are still more strongly populated. Thus, for all targets and bombarding energies, the order of preference for 3-body decay channels is: 1) one heavy and two light fragments (vertices), 2) two medium sized and one light fragment (sides of triangle), and 3)

three equal sized fragments (center). As the available energy in the center of mass system increases, the 3-body decays become more probable and the different 3-body decay channels are populated more evenly.

4-4 Excitation functions

Valuable information can be obtained from the "excitation functions" of n-fold events. Different models have been proposed, that predict a sudden rise in the multibody probability for an excitation energy between 3 and 5 MeV/u, as a signature for the onset of multifragmentation [31,32]. These excitation functions can be obtained at a given fixed bombarding energy from the source velocity distributions, since the widths of these distributions have been shown to be effectively related to a continuous range of incomplete fusion processes.

The relative abundances of binary, ternary, quaternary etc., events were determined for different bins of the source velocity, and thus of the corresponding mass and excitation energy of the source. Fig. 29 presents the "excitation functions" for the multifold events, obtained from the source velocity distributions, for the different systems at 35, 40, 45 and 55 MeV/u. P(n) represents the proportion of n-fold events with respect to the total number of coincidence events: P(n) = N(n)/[N(2)+N(3)+N(4)+...], where N(n) is the number of n-fold events. Evaporation residues, corresponding to n=1, were not considered, since in reverse kinematics they are confined to a very small angle around the beam direction, where the detection efficiency is small. Rather than plotting these probabilities directly as a function of the source velocity, we have chosen to plot them versus the quantity:

$$Q = (E/A)_{beam} x (V_{source}/ V_{beam}) x (1-V_{source}/V_{beam}).$$

This has the purpose of removing as much as possible the bombarding energy dependence. The quantity Q corresponds to the excitation energy per nucleon in a simple incomplete fusion model. Because such a model does not take into account preequilibrium particle emission processes, the quantity Q may be considered as an upper limit of the true

excitation energy. We have estimated, by means of a dynamical code [33], that the uncertainty on the horizontal scale connected to the emission of preequilibrium nucleons is at most around 30% for the systems considered in this study. Therefore the semi-quantitative analysis presented below should not be strongly affected by such preequilibrium emission processes.

The excitation functions presented in fig. 29 exhibit several remarkable features. The excitation energies obtained with this procedure are stunning, as they extend up to 9 MeV/u! Thus, we maybe producing "nuclear systems" with excitation energies larger that their total binding energy.

The probabilities for three, four, and 5-fold events increase substantially as a function of the quantity Q. Such behavior suggests that there is indeed a strong connection between the source velocity and excitation energy, since the multifragment decay probability is expected to increase dramatically with excitation energy. The strong dependence of the branching ratios on the calculated excitation energy also confirms that the width of the velocity distribution is mostly due to the reaction dynamics, and is only partly due to evaporative broadening. Actually, if evaporation processes were the only source of broadening, these excitation functions should be flat. A similar increase in the multiplicity of intermediate mass fragments has been observed recently at 50 MeV/u [19] and also at much higher incident energy [20], where the average multiplicity of complex fragments increases up to an excitation energy of 8 MeV/u, and decreases at higher excitation energies.

The rate of multifold events increases smoothly with the quantity Q, up to approximately 6-8 MeV/u, without showing any discontinuity. The statistical multifragmentation calculations of Bondorf et al. [31] predict a sudden rise in the multibody probability at an excitation energy of about 3 MeV/u for a nucleus of mass 100. Gross et al. predict a similar transition to nuclear cracking at about 5 MeV/u for the ^{131}Xe nucleus [32]. However, it would be necessary to filter such calculations by our detection acceptance in order to make a valid comparison.

A most remarkable result is that, at any given bombarding energy, these excitation functions are almost identical for all targets. Even more extraordinary is that these excitation functions are almost independent on the bombarding energy. This suggests that the competition between the various multifragment channels is independent of the entrance channel. More precisely, at a given bombarding energy, the similarity between the excitation functions for the different targets indicates that the sources produced in these reactions can be characterized mainly from the amount of mass picked up by the projectile from the target, and depend relatively little on the actual nature of the target.

In the standard incomplete fusion model, the excitation energy depends essentially on the mass that has been picked-up. A similar statement can also be made about angular momentum. This is true at any given bombarding energy. However, the angular momentum at fixed excitation energy should decrease with increasing bombarding energy like $(E/A)^{-1/2}$. Over the range 35 to 55 MeV/u, the overall angular momentum decrease is about 25%. Therefore the incomplete fusion model suggests that the excitation functions should be directly comparable to one another in terms of the excitation energies and, to a somewhat lower extent, of the angular momentum. To summarize, it appears that, no matter what is the bombarding energy, once the excitation energy (and the angular momentum) is determined from the source velocity, the resulting branching ratios for the various multifragment channels are fixed. This suggests that statistics play an important role in multifragmentation.

A closer look at fig. 29 shows some discrepancies for the ^{12}C target, for which the multifold probabilities are systematically lower than the heavier targets. One possible explanation for these differences is the broadening of the excitation energy bins due to light-particle evaporation. This is particularly severe in the case of ^{12}C for which evaporation is mostly responsible for the width of the source velocity, as mentioned before. This could also explain why at the highest excitation energies the multifold probabilities for the ^{27}Al target, which are in the tail of the source velocity distribution, fall slightly below those measured for the heavier targets. The relative importance of the primary effects (incomplete fusion

processes) and secondary effects (light particle evaporation), which both contribute to the width of the source velocity distribution, can indeed be very different in the wings of the distribution and in the peak. The flattening observed in the case of the ^{27}Al target at high excitation energy may therefore be explained if only secondary effects contribute to the wings. (Moreover, as already mentioned, an additional source of the differences for the various targets could be that the sources are formed with slightly different angular momenta.)

These multifold probabilities have not been corrected for detection efficiency. It is therefore necessary to verify that the observed excitation functions are not strongly biased by some experimental artifact. In order to evaluate the influence of the detection acceptance on our results, Monte-Carlo calculations were performed for the 35 MeV/u $^{139}La + ^{40}Ca$ reaction. We generated sets of 2-, 3- and 4-fold events, striving to reproduce as well as possible the experimental charge, angular and velocity distributions. In particular, we took into account the fact that the angular distributions of light fragments are backward peaked in the center of mass, and that their center-of-mass velocities are larger in the backward than in the forward direction. These events were then filtered by the detector acceptance in order to estimate the contamination due to incompletely detected events. In the case of the ^{40}Ca target at 35 MeV/u the contamination of the detected 2- and 3-fold events by incompletely detected higher multiplicity events is found to be approximately 20%, when a gate is set on a total detected charge greater than 30. This contamination level should be higher for the heavier targets, and lower for the lighter targets, and should increase with the incident energy.

In order to investigate the influence of this contamination on the excitation functions, a simulation was performed where the source velocity distribution of the measured 4-fold events was assigned to events of all multiplicities, thereby simulating flat excitation functions. After filtering by the detector acceptance, the calculated excitation functions along with the data for the 35 MeV/u $^{139}La + ^{40}Ca$ reaction are shown in Fig. 30. The calculated excitation functions for the 3- and 4-fold events are essentially flat, with the 4-fold events

dropping slightly at small excitation energies. In contrast, the experimental data rises rapidly with excitation energy. Therefore the detection efficiency does not seem to bias the measured excitation functions in any significant way.

5-Summary and Conclusions

The data presented in this paper illustrate the dramatic change in the experimental complex fragment production between 18 and 55 MeV/u. Below 30 MeV/u, the main features of these reactions have been successfully explained in the framework of the incomplete-fusion compound-nucleus statistical-decay model. In this case, aside from spectators and projectile- & target-like deep inelastic products, the complex fragments are produced in highly equilibrated binary processes, which give rise to flat or forward-backward symmetric angular distributions, well defined Coulomb circles, and 2-fold coincidences which sum to a nearly constant charge. At higher energies, this simple picture fails to reproduce the data: the angular distributions exhibit a strong non-isotropic component for all Z-values, the Coulomb circles are smeared out, the centroids of the coincidence charge distributions decrease and their widths increase as the target mass increases (at a given energy). The bombarding energy at which this transition occurs depends on the entrance-channel-mass asymmetry of the system, decreasing as the mass of the target increases. For example, for targets as heavy or heavier than ^{51}V, the binary features have already completely disappeared at 35 MeV/u. In contrast, for the light ^{27}Al target, the binary ridge line in the $Z_1 + Z_2$ plots can still be observed at 45 MeV/u. The disappearance of the characteristic binary signatures, together with other experimental evidence, suggests an increasing importance of multifragment emission processes for the higher beam energies and more symmetric entrance channels.

The excitation functions for multifragment events rise strongly with excitation energy. Their independence from the target-projectile combination and from the bombarding energy is rather striking, and suggests an intermediate nuclear system whose decay properties depend mainly on its excitation energy and angular momentum. However in such a study, it would be

useful to have an independent estimate of the deposited excitation energy, since this cannot be extracted too precisely from the source velocity. Neutron multiplicity measurements [34], or light charged particle multiplicity [19] can provide such an independent determination of the excitation energy.

References

[1] L.G. Moretto and G.J. Wozniak, Prog. Part. & Nucl. Phys. **21** (1988) 401, and references therein

[2] M.A. McMahan, L.G. Moretto, M.L. Padgett, G.J. Wozniak, L.G. Sobotka and M.G. Mustafa, Phys. Rev. Lett. **54** (1985) 1995

[3] D. N. Delis, Y. Blumenfeld, D. R. Bowman, N. Colonna, K. Hanold, K. Jing, M. Justice, J. C. Meng, G. F. Peaslee, G. J. Wozniak, and L. G. Moretto, Z. Phys. **A339** (1991) 279

[4] D. N. Delis, Y. Blumenfeld, D. R. Bowman, N. Colonna, K. Hanold, K. Jing, M. Justice, J. C. Meng, G. F. Peaslee, G. J. Wozniak, and L. G. Moretto, Nucl. Phys. **A534** (1991) 403

[5] G. Auger, D. Jouan, E. Plagnol, F. Pougheon, F. Naulin, H. Doubre and C. Gregoire, Z. Phys. **A321** (1985) 243

[6] R.J. Charity, M.A. McMahan, D.R. Bowman, Z.H. Liu, R.J. McDonald, G.J. Wozniak, L.G. Moretto, S. Bradley, W.L. Kehoe, A.C. Mignerey and M.N. Nambodiri, Phys. Rev. Lett. **56** (1986) 1354

[7] F. Auger, B. Berthier, A. Cunsolo, A. Foti, W. Mittig, J.M. Pascaud, E. Plagnol, J. Quebert, and J.P. Wieleczko, Phys. Rev. **C35** (1987) 190.

[8] R.J. Charity, D.R. Bowman, Z.H. Liu, R.J. McDonald, M.A. McMahan, G.J. Wozniak, L.G. Moretto, S. Bradley, W.L. Kehoe and A.C. Mignerey, Nucl. Phys. **A476** (1988) 516

[9] R. J. Charity, M.A. McMahan, G.J. Wozniak, R.J. McDonald, L.G. Moretto, D.G. Sarantities, L.G. Sobotka, G. Guarino, A. Pantaleo, L. Fiore, A. Gobbi and K.D. Hildenbrand, Nucl. Phys. **A483** (1988) 371

[10] H.Y. Han, K.X. Jing, E. Plagnol, D.R. Bowman, R.J. Charity, L. Vinet, G.J. Wozniak and L.G. Moretto, Nucl. Phys. **A492** (1989) 138

[11] E. Plagnol, L. Vinet, D.R. Bowman, Y.D. Chan, R.J. Charity, E. Chavez, S.B. Gazes, H. Han, W.L. Kehoe, M.A. McMahan, L.G. Moretto, R.G. Stokstad, G.J. Wozniak and G. Auger, Phys. Lett. **B221** (1989) 11

[12] R.J. Charity, K.X. Jing, D.R. Bowman, M.A. McMahan, G.J. Wozniak, L.G. Moretto, N. Colonna, G. Guarino, A. Pantaleo, L. Fiore, A. Gobbi, and K.D. Hildenbrand, Nucl. Phys. **A511** (1990) 59.

[13] D.R. Bowman, G.F. Peaslee, N. Colonna, R.J. Charity, M.A. McMahan, D. Delis, H.Han, K. Jing, G.J. Wozniak, L.G. Moretto, W.L. Kehoe, B. Libby, A.C. Mignerey, A. Moroni, S. Angius, I. Iori, A. Pantaleo, and G. Guarino, Nucl. Phys. **A523** (1991) 386.

[14] N. Colonna, R.J. Charity, D.R. Bowman, M.A. McMahan, G.J. Wozniak, L.G. Moretto, G.Guarino, A. Pantaleo, L. Fiore, A. Gobbi and K.D. Hildenbrand, Phys. Rev. Lett. **62** (1989) 1833.

[15] R. Bougault, J. Colin, F. Delaunay, A. Genoux-Lubain, A. Hajfani, C. Lebrun, J.F. Lecolley, M. Louvel, and J.C. Steckmeyer, Phys. Lett. **B232** (1989) 291.

[16] Y.D. Kim, M.B. Tsang, C.K. Gelbke, W.G. Lynch, N. Carlin, Z. Chen, R. Fox, W.G. Gong, T. Mukarami, T.K. Nayak, R.M. Ronningen, H.M. Xu, F. Zhu, and W. Bauer, Phys. Rev. Lett. **63** (1989) 494.

[17] R. Trockel, K.D. Hildenbrand, U. Lynen, W.F.J. Muller, H.J. Rabe, H. Sann, H. Stelzer, W. Trautmann, R. Wada, E. Eckert, P. Kreutz, A. Kuhlmichel, J. Pochodzalla, and D. Pelte, Phys. Rev. **C39** (1989) 729.

[18] Y. Blumenfeld, N. Colonna, P. Roussel-Chomaz, D.N. Delis, K. Hanold, J.C. Meng, G.F. Peaslee, Q.C. Sui, G.J. Wozniak, L.G. Moretto, B. Libby, A. C. Mignerey, G. Guarino, N. Santoruvo and I. Iori, Phys. Rev. Lett. **66** (1991) 576.

[19] D.R. Bowman, G.F. Peaslee, R.T. de Souza, N. Carlin, C.K. Gelbke, W.G. Gong, Y.D. Kim, M.A. Lisa, W.G. Lynch, L.Phair, M.B. Tsang, C. Williams, N. Colonna, K. Hanold, M.A. McMahan, G.J. Wozniak, L.G. Moretto, and W.A. Friedman, Phys. Rev. Lett. **67** (1991) 1527.

[20] C.A. Ogilvie, J.C. Adloff, M. Begemann-Blaich, P. Bouissou, J. Hubele, G. Imme, P. Kreutz, G.J. Kunde, S. Leray, V. Lindenstruth, Z.Liu, U. Lynen, R.J. Meijer, U. Milkau, W.F.J. Müller, C. Ngo, J. Pochodzalla, G. Raciti, G. Rudolf, H. Sann, A. Schüttauf, W. Seidel, L. Stuttge, W. Trautmann, and A. Tucholski, Phys. Rev. Lett. **67** (1991) 1214

[21] K. Hagel, M. Gonin, R. Wada, J. B. Natowitz, B. H. Sa, Y. Lou, M. Gui, D. Utley, G. Nebbia, D. Fabris, G. Prete, J. Ruiz, D. Drain, B Chambon, B. Cheynis, D. Guinet, X. C. Hu, A. Demeyer, C. Pastor, A. Giorni, A. Lleres, P. Stassi, J. B. Viano, and P. Gonthier, Phys. Rev. Lett. **68** (1992) 2141.

[22] N. Colonna, P. Roussel-Chomaz, N. Colonna, M. Di Toro, L.G. Moretto and G.J. Wozniak, preprint LBL-30810, Phys. Lett. B, in press.

[23] N. Colonna et al., to be published.

[24] W.L. Kehoe, A. C. Mignerey, A. Moroni, I. Iori, G.F. Peaslee, N. Colonna, K. Hanold, D.R. Bowman, L.G. Moretto, M.A. McMahan, J.T. Walton and G.J. Wozniak, Nucl. Instr. and Meth. **A311** (1992) 258

[25] J. T. Walton, H. A. Sommer, G. J. Wozniak, G. F. Peaslee, D. R. Bowman, W. L. Kehoe, and A. Moroni, IEEE Trans. on Nucl. Sci. **37** (1990) 1578

[26] M. A. Mahan, G. J. Wozniak, C. M. Lyneis, D. R. Bowman, R. J. Charity, Z. H. Liu, L. G. Moretto, W. L. Kehoe, A. C. Mignerey and M. N. Namboodiri, Nucl. Instr. & Meth. **A253** (1986) 1.

[27] J. B. Moulton, J.E. Stephenson, R.P. Schmitt, and G.J. Wozniak, Nucl. Instr. and Meth. **157** (1978) 325

[28] D. R. Bowman, W.L. Kehoe, R. J. Charity, M. A. McMahan, A. Moroni, A. Bracco, S. Bradley, I, Iori, R. J. McDonald, A. C. Mignerey, L. G. Moretto, M. N. Namboodiri, and G. J. Wozniak, Phys. Lett **B189** (1987) 282

[29] U.L. Businaro and S. Gallone, Nuovo Cim. **1** (1955) 629,1277

[30] K. Hanold, L. G. Moretto, G. F. Peaslee, D. R. Bowman, M. F. Mohar, and D. J. Morrissey, Lawrence Berkeley Laboratory preprint LBL-

[31] J. Bondorf, R. Donangelo, I.N. Mishustin and H. Schulz, Nucl. Phys. **A444** (1985) 460.

[32] D.H.E. Gross, Yu-ming Zheng, and H. Massman, Phys. Lett. **B200** (1987) 397.

[33] A. Bonasera, M. Colonna, M. Di Toro, F. Gulminelli and H.H. Wolter, Phys. Lett. **B244** (1990) 169, and references therein

[34] J. Galin, Proc. of XXIst Summer School on Nuclear Physics Mikolajki(Poland), IOP Publishing Limited and references therein.

Figure Captions

Fig. 1 Schematic drawing of the experimental set-up which consisted of two 3x3 arrays of 3-element Si-Si-Plastic telescopes, placed on opposite sides of the beam. In the lower portion of the figure an exploded view of one of the telescopes is shown.

Fig. 2 Energy spectrum of a 5 mm Si detector exposed to a quadruplet beam of 45 MeV/u $^{14}N^{4+}$, $^{28}Si^{8+}$, $^{56}Fe^{16+}$, and Kr^{24+} ions from the Bevalac.

Fig. 3 Particle identification spectra for the $^{139}La + ^{40}Ca$ reaction at 40 MeV/u shown in both linear (upper) and logarithmic (lower) representations. The individual peaks correspond to different elements.

Fig. 4 Experimental cross section ($d^2\sigma/dV_{\parallel}dV_{\perp}$) in the $V_{\parallel}$-$V_{\perp}$ plane for representative Z-values between 5 and 50 for the 40 MeV/u $^{139}La + ^{12}C$ reaction.

Fig. 5 Same as fig. 4 for the 40 MeV/u $^{139}La + ^{27}Al$ reaction.

Fig. 6 Same as fig. 4 for the 55 MeV/u $^{139}La + ^{27}Al$ reaction. The cut at large V_{Lab} for the lightest fragments (Z = 5) corresponds to the threshold in the ΔE detectors.

Fig. 7 Same as fig. 4 for the 40 MeV/u $^{139}La + ^{nat}Cu$ reaction.

Fig. 8 Same as fig. 4 for the 55 MeV/u $^{139}La + ^{nat}Cu$ reaction.

Fig. 9 Average source velocity (normalized to the beam velocity) as a function of the charge (Z) of the detected fragment, for four incident energies and several targets.

Fig. 10 Average emission velocity in the source frame, as a function of the charge of the detected fragments, for four incident energies and several targets.

Fig. 11 Angular distributions ($d\sigma/d\Theta$) in the source frame for representative Z-values from the 40 MeV/u ^{139}La + X reactions. The Z-values and normalization factors are indicated for each set of points. The curves are fits to the data points.

Fig. 12 Same as fig. 11 at 45 MeV/u.

Fig. 13 Same as fig. 11 at 55 MeV/u.

Fig. 14 Angle-integrated cross sections of products from the 40 MeV/u ^{139}La + X reactions. In all cases the statistical errors are smaller than the size of the data points. The error bars shown are estimates of the systematic error in fitting the angular distributions (see text).

Fig. 15 Same as fig. 14 at 45 MeV/u.

Fig. 16 Same as fig. 14 at 55 MeV/u.

Fig. 17 Contour plots of the extracted source velocity (V_s) versus total detected charge ($Z_1 + Z_2$) for the 2-fold coincidence events, for the 18 MeV/u $^{139}La + ^{12}C$, ^{27}Al, ^{48}Ti and ^{64}Ni reactions and 26 and 31 MeV/u $^{129}Xe + ^{12}C$, ^{27}Al, ^{48}Ti and ^{nat}Cu reactions. The beam energy and the target are indicated in the first row and column, respectively. The total available energy in the center-of-mass system is indicated in the lower right of each frame. The horizontal lines indicate the complete fusion velocity for each system and the vertical arrow the projectile charge.

Fig. 18 Same as fig. 17 for the 35, 40, 45, and 55 MeV/u $^{139}La + ^{12}C$, ^{27}Al, ^{51}V, and ^{nat}Cu reactions.

Fig. 19 Schematic representation of the effect of light charged-particle evaporation on the correlation between the source velocity and total detected charge. The thick solid curve represents the correlation for the primary fragments. Going from the right to the left the three dashed lines represent cases of low, moderate and high excitation energy, respectively, which corresponds to increasing amounts of light charge particle emission.

Fig. 20 Linear contour plots of the correlation between Z_1 and Z_2 for the 2-fold coincidence events from the 18 MeV/u $^{139}La + ^{12}C$, ^{27}Al, ^{48}Ti and ^{64}Ni reactions and 26 and 31 MeV/u $^{129}Xe + ^{12}C$, ^{27}Al, ^{48}Ti and ^{nat}Cu reactions. The distributions have been symmetrized by randomly assigning Z_1 and Z_2.

Fig. 21 Same as fig. 20 for the 35, 40, 45, and 55 MeV/u $^{139}La + ^{12}C$, ^{27}Al, ^{51}V, and ^{nat}Cu reactions.

Fig. 22 Total detected charge for the 40 MeV/u $^{139}La + ^{12}C$, ^{27}Al, ^{51}V, and ^{nat}Cu reactions; row 1, inclusive charge; row 2, 2-fold events; row 3, 3-fold events, and row 4, 4-fold events.

Fig. 23 Same as fig. 22 for the 45 MeV/u $^{139}La + ^{27}Al$, ^{51}V, ^{nat}Cu and ^{139}La reactions.

Fig. 24 Same as fig. 23 for the 55 MeV/u reactions.

Fig. 25 Source velocity distributions for the 40 MeV/u $^{139}La + ^{12}C$, ^{27}Al, ^{51}V, and ^{nat}Cu reactions, and for different numbers of detected fragments. Only events with a total detected charge larger than 30 are represented. The source velocity is normalized to the beam velocity.

Fig. 26 Same as fig. 25 for the 45 MeV/u $^{139}La + ^{27}Al$, ^{51}V, ^{nat}Cu and ^{139}La reactions.

Fig. 27 Same as fig. 26 for the 55 MeV/u reactions.

Fig. 28 Dalitz plots for the three-body events for the 35, 40 and 55 MeV/u $^{139}La + ^{27}Al$, ^{51}V, ^{nat}Cu and ^{139}La reactions. The y-axis is the ratio Z_1/Z_{total}. The x-axis is given by: $\tan 30^\circ \times (Z_2/Z_{total}) + (Z_3/Z_{total})/\sin 60^\circ = 0.577 \times (Z_2/Z_{total}) + 1.155 (Z_3/Z_{total})$. The detected fragments have been randomized so that there is no preferred ordering of Z_1, Z_2 and Z_3.

Fig. 29 Proportion of 2-, 3-, 4- and 5-fold events as a function of excitation energy per nucleon (Q, see text) for the different targets (symbols, see inset) studied at E_{lab}=35 (upper left), 40 (lower left), 45 (upper right), and 55 MeV/u (lower right).

Fig. 30 Simulation (upper) and experimental data (lower) percentage of 2-, 3-, and 4-fold events as a function of excitation energy per nucleon for the 35 MeV/u $^{139}La + ^{40}Ca$ reaction.

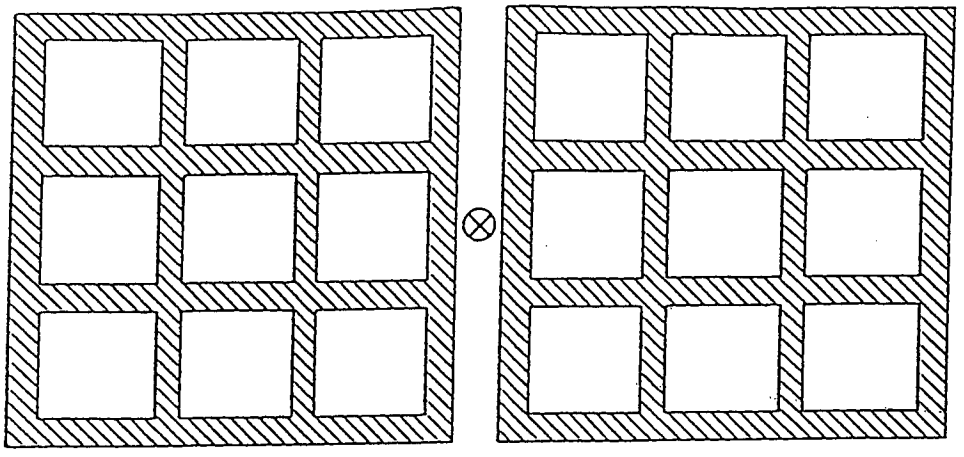

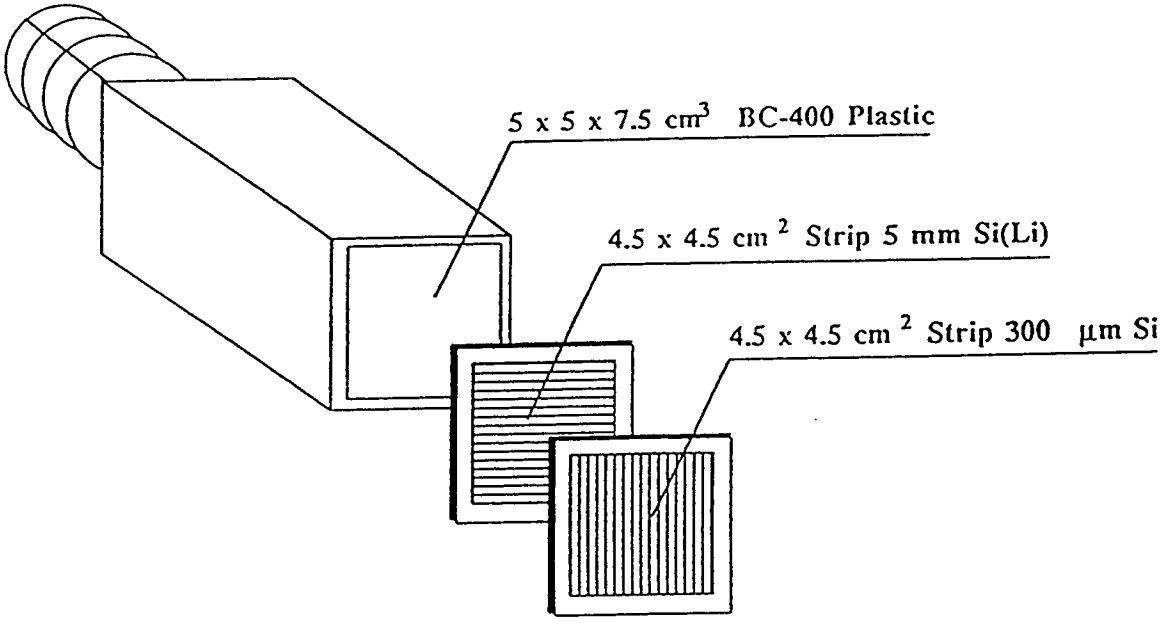
5 x 5 x 7.5 cm3 BC-400 Plastic
4.5 x 4.5 cm 2 Strip 5 mm Si(Li)
4.5 x 4.5 cm 2 Strip 300 µm Si

XBL 921-182

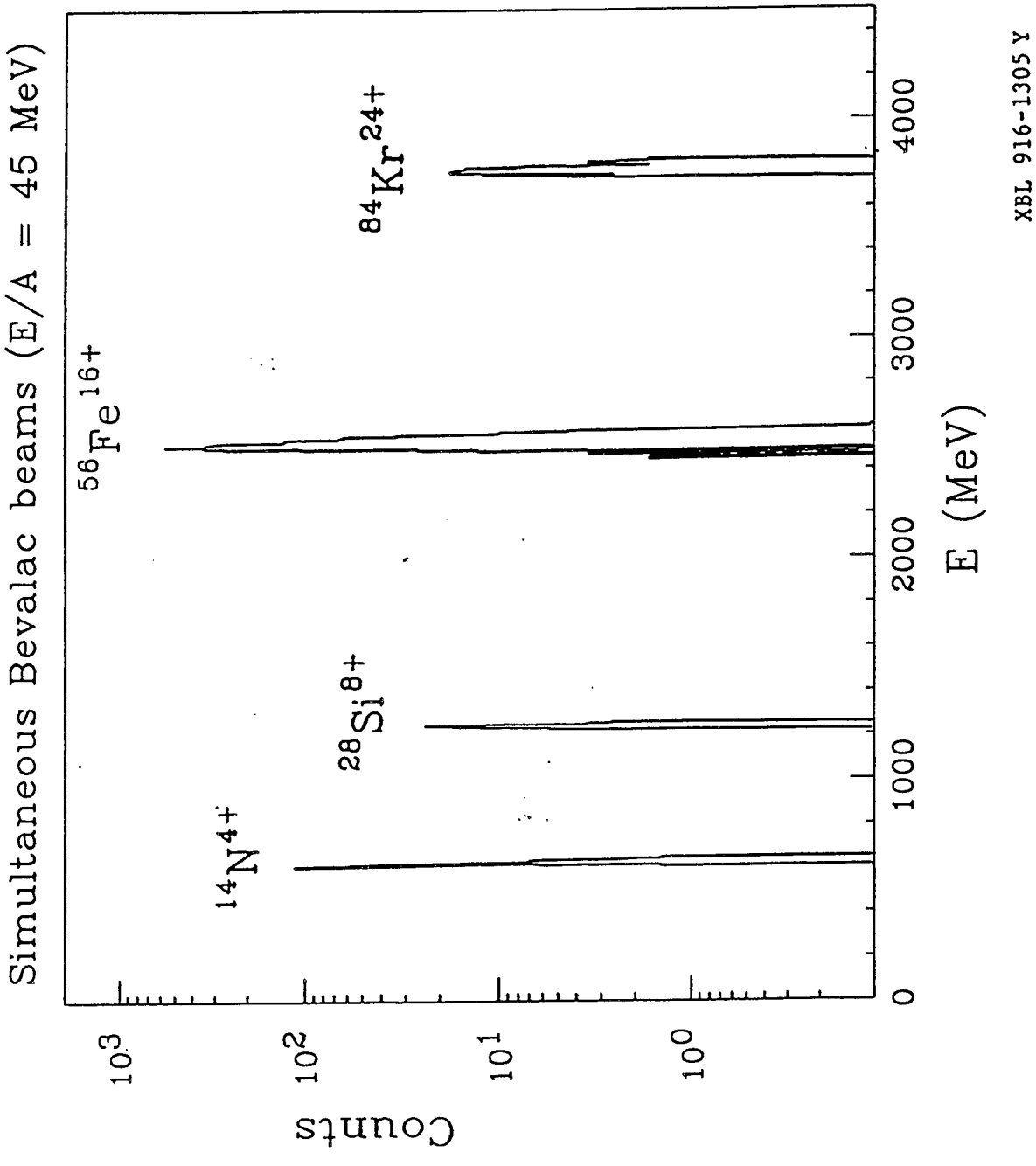

XBL 916-1305 Y

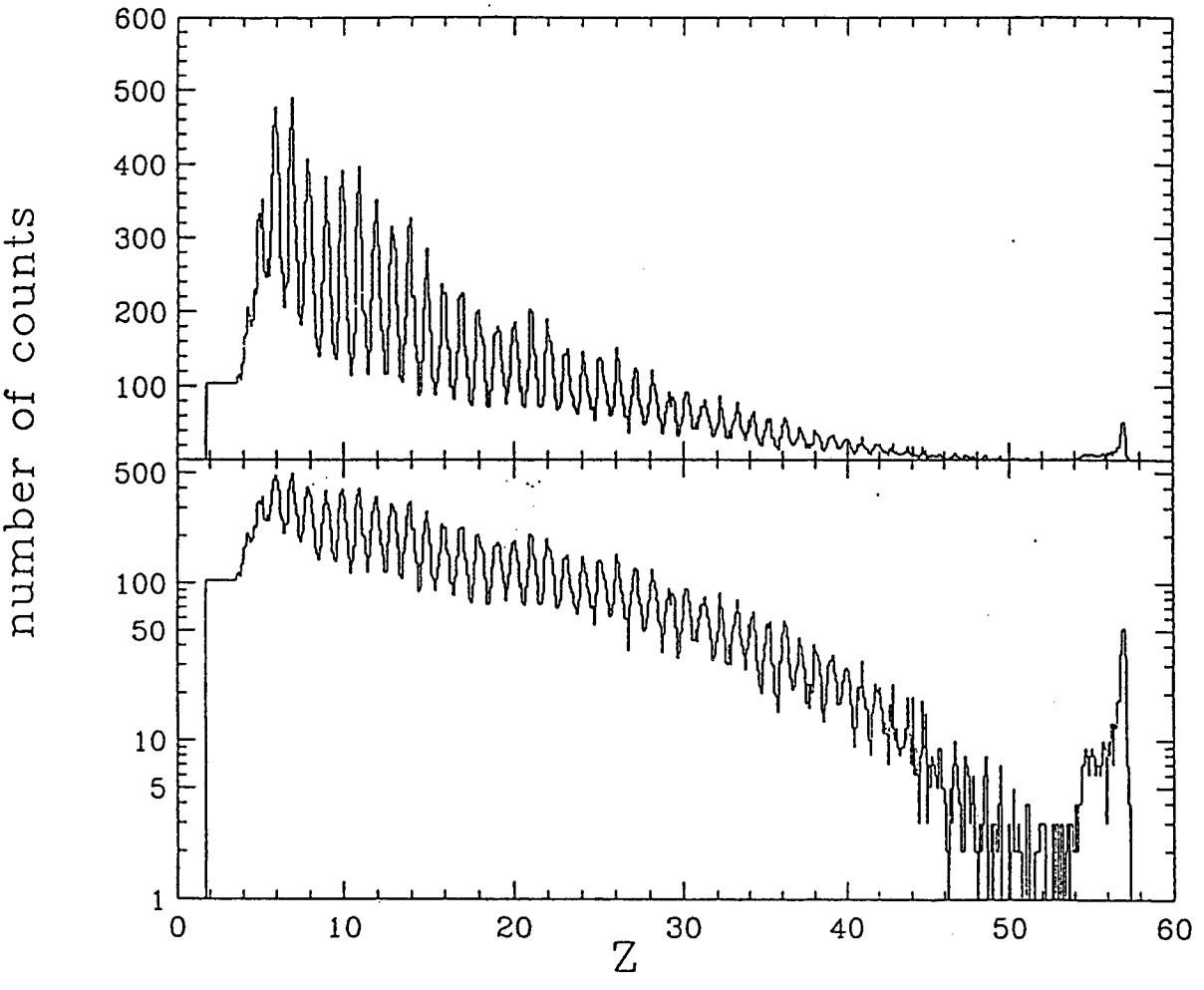
number of counts
600
500
400
300
200
100
500
100
50
10
5
1
0
10
20
30
40
50
60
Z

XBL 921-181

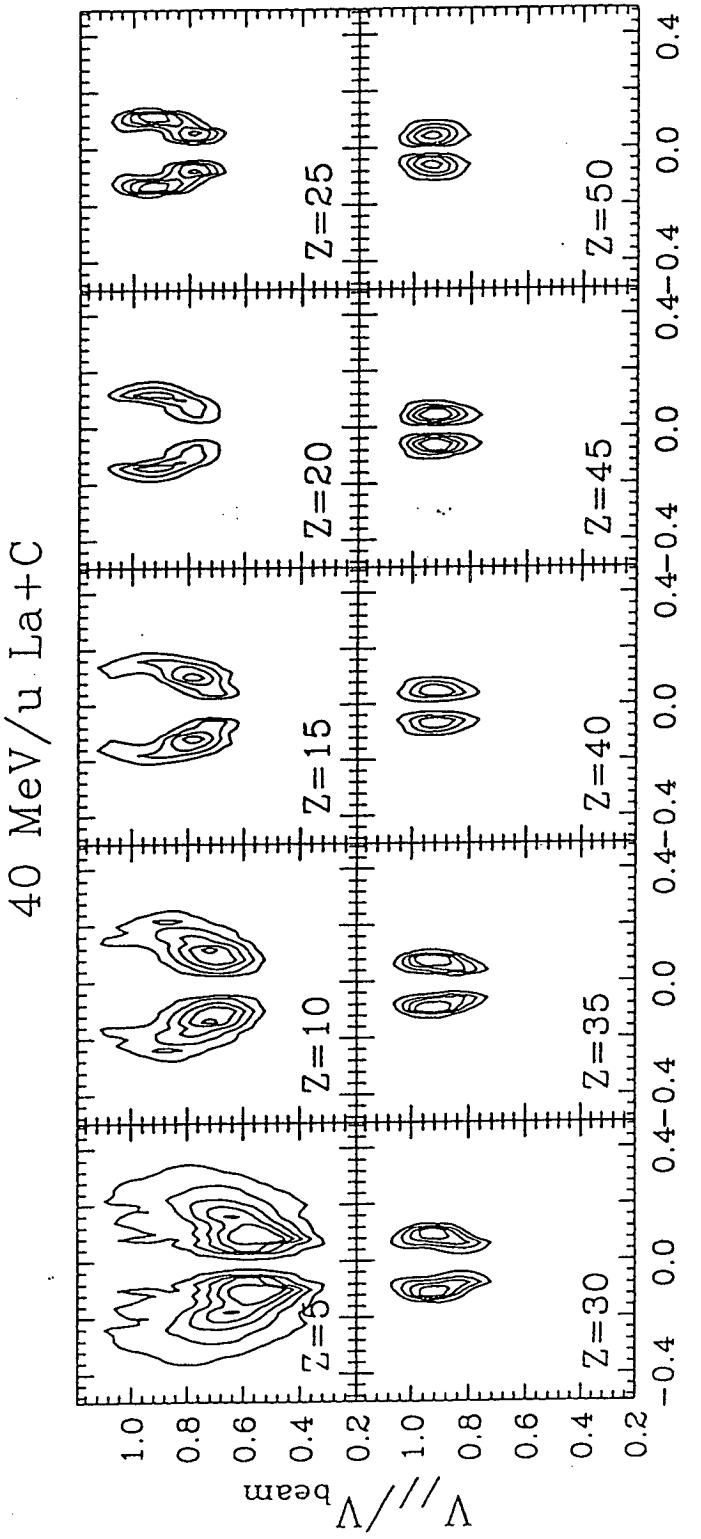
40 MeV/u La+C
Z=5
Z=10
Z=15
Z=20
Z=25
Z=30
Z=35
Z=40
Z=45
Z=50
$V_{//}/V_{beam}$
$V_{\perp}/V_{beam}$
XBL 921-180

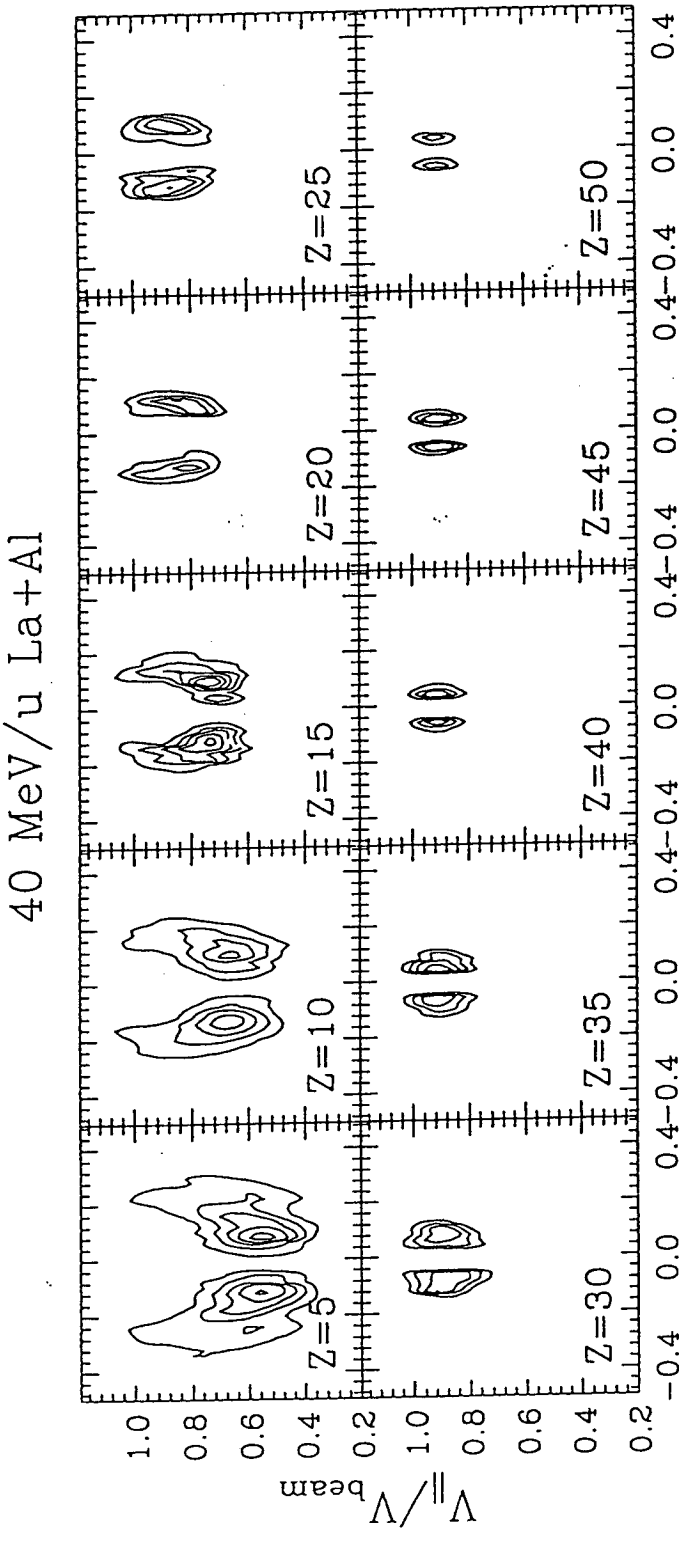
40 MeV/u La+Al
Z=5
Z=10
Z=15
Z=20
Z=25
Z=30
Z=35
Z=40
Z=45
Z=50
$V_{\parallel}/V_{beam}$
$V_{\perp}/V_{beam}$
XBL 921-179

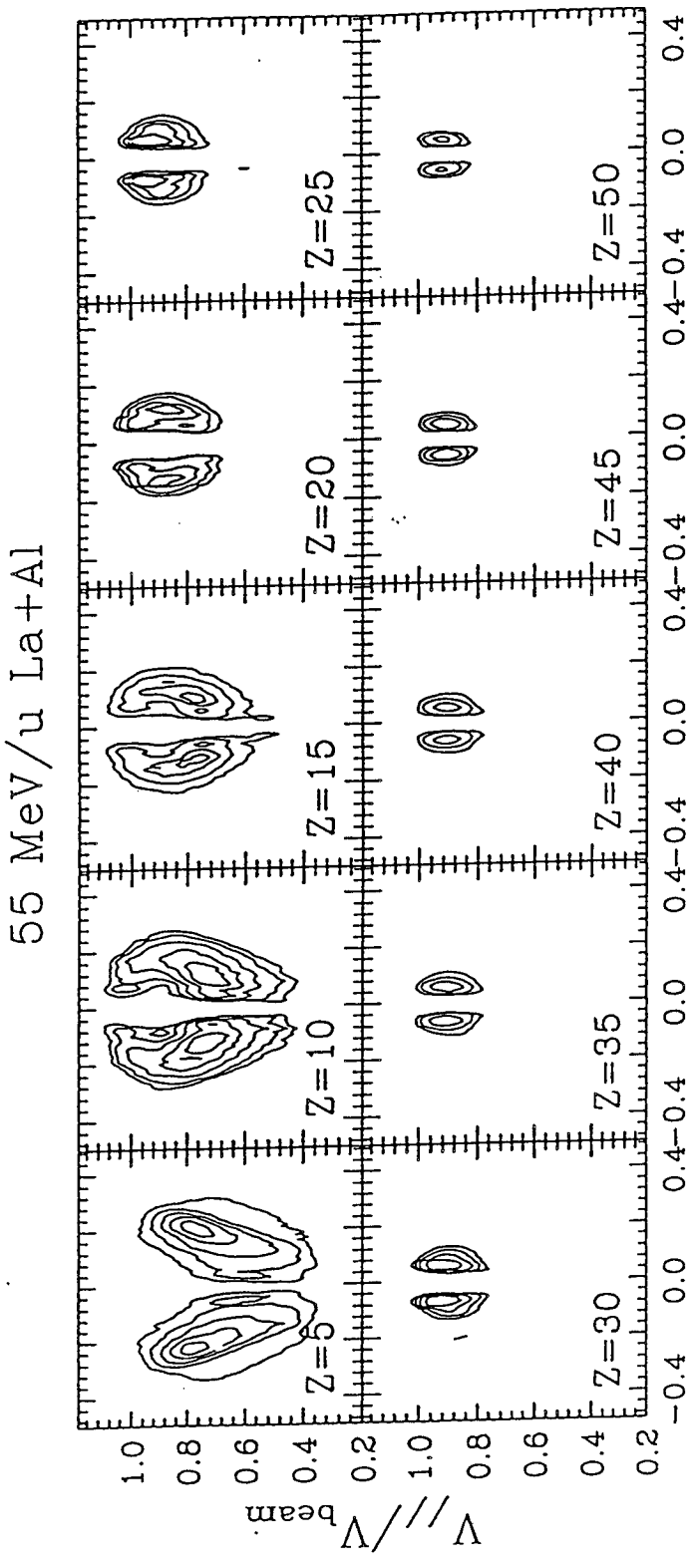
55 MeV/u La+Al
Z=5
Z=10
Z=15
Z=20
Z=25
Z=30
Z=35
Z=40
Z=45
Z=50
$V_{//}/V_{beam}$
$V_{\perp}/V_{beam}$
XBL 921-178

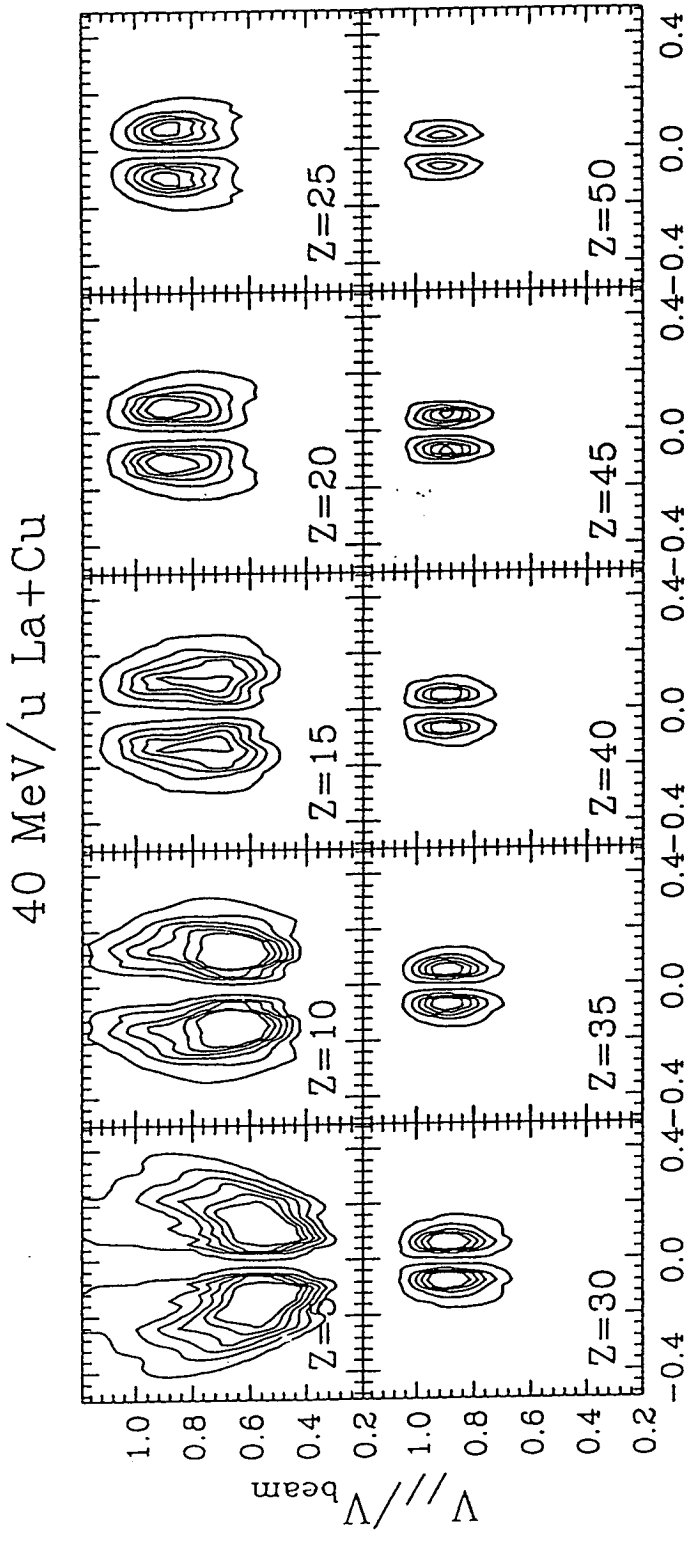
40 MeV/u La+Cu
Z=5
Z=10
Z=15
Z=20
Z=25
Z=30
Z=35
Z=40
Z=45
Z=50
$V_{//}/V_{beam}$
$V_{\perp}/V_{beam}$
1.0
0.8
0.6
0.4
0.2
-0.4
0.0
0.4

XBL 921-177

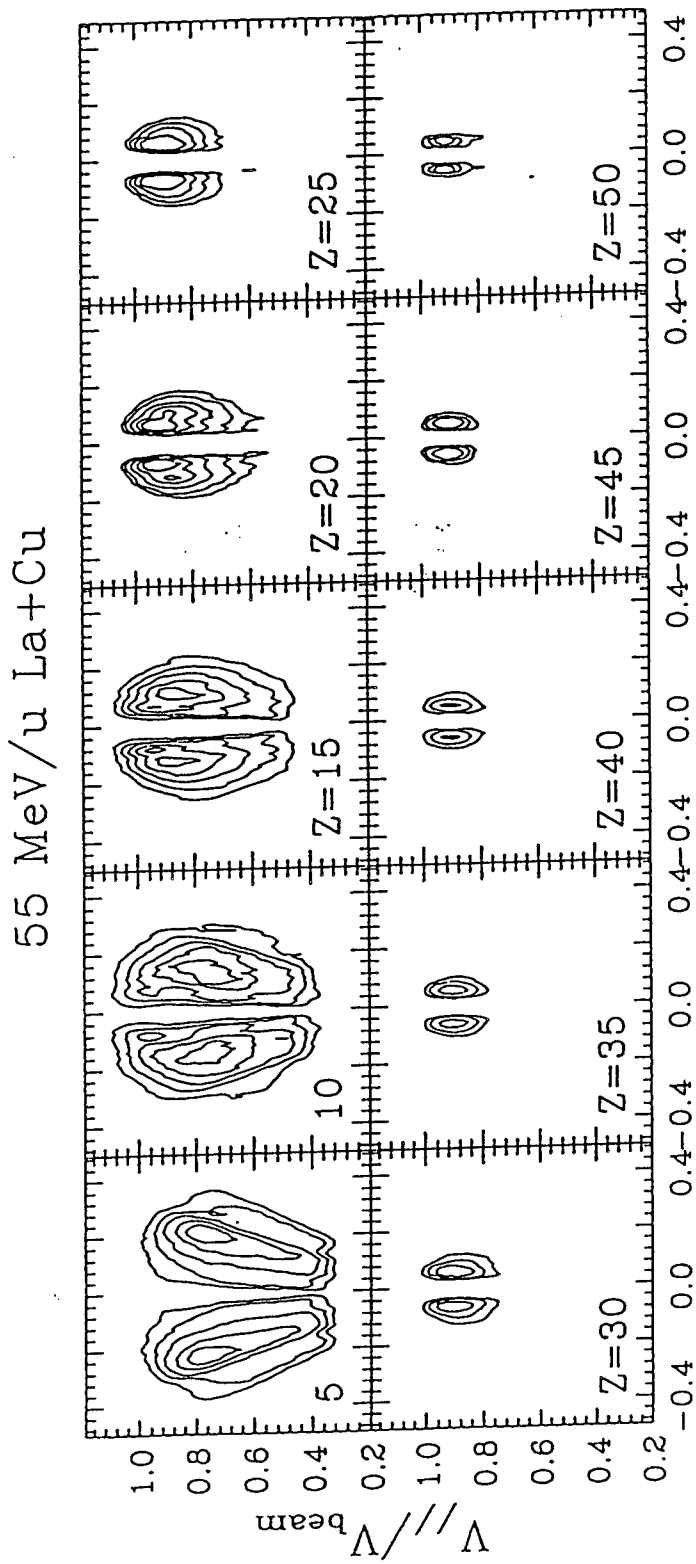
55 MeV/u La+Cu
Z=5
Z=10
Z=15
Z=20
Z=25
Z=30
Z=35
Z=40
Z=45
Z=50
$V_{///}/V_{beam}$
$V_{\perp}/V_{beam}$
XBL 921-176

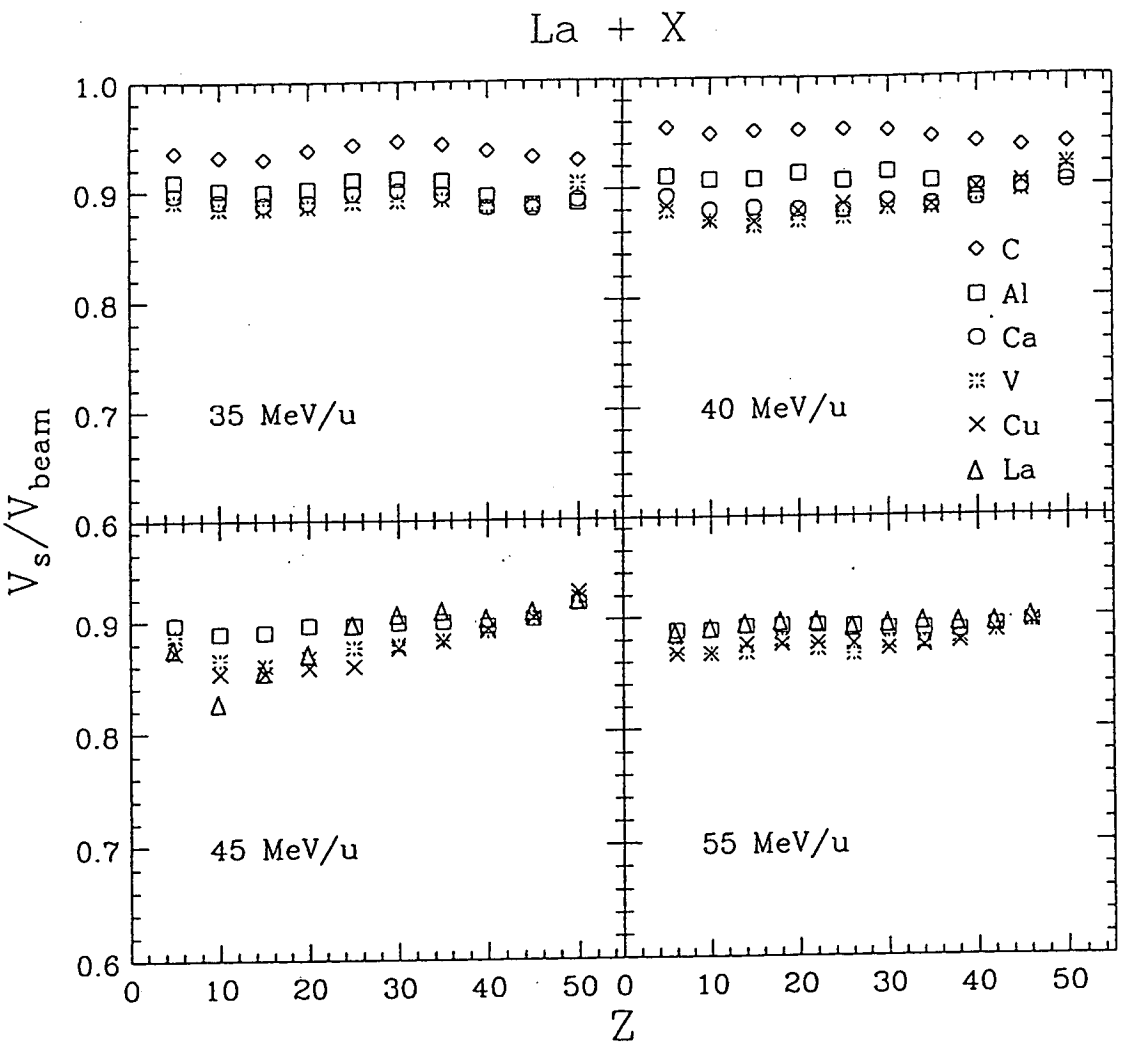
La + X
1.0
0.9
0.8
0.7
0.6
V_s/V_{beam}
35 MeV/u
40 MeV/u
45 MeV/u
55 MeV/u
C
Al
Ca
V
Cu
La
0
10
20
30
40
50
Z

XBL 921-175

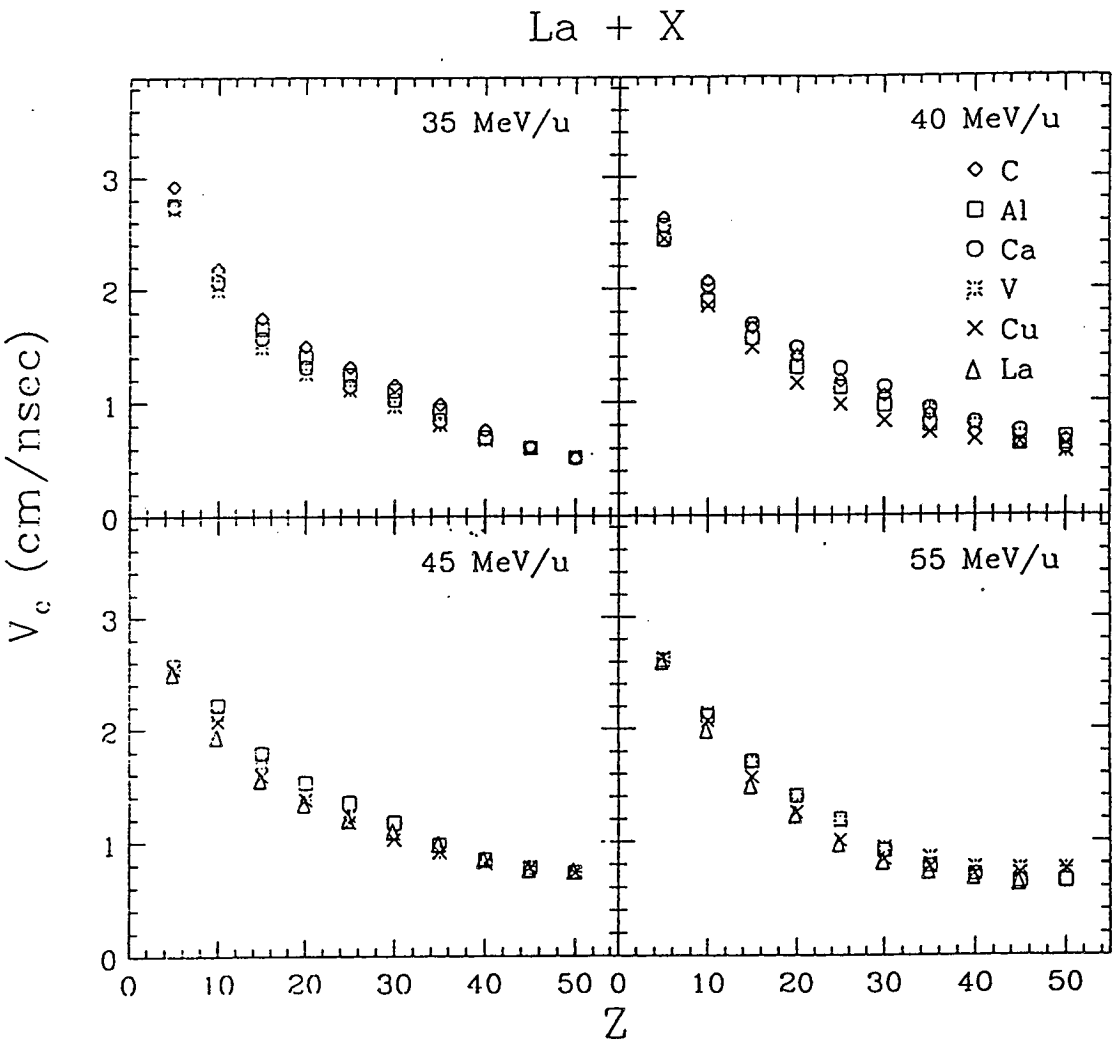
La + X
35 MeV/u
40 MeV/u
45 MeV/u
55 MeV/u
C
Al
Ca
V
Cu
La
V_c (cm/nsec)
Z
0
10
20
30
40
50
1
2
3

XBL 921-174

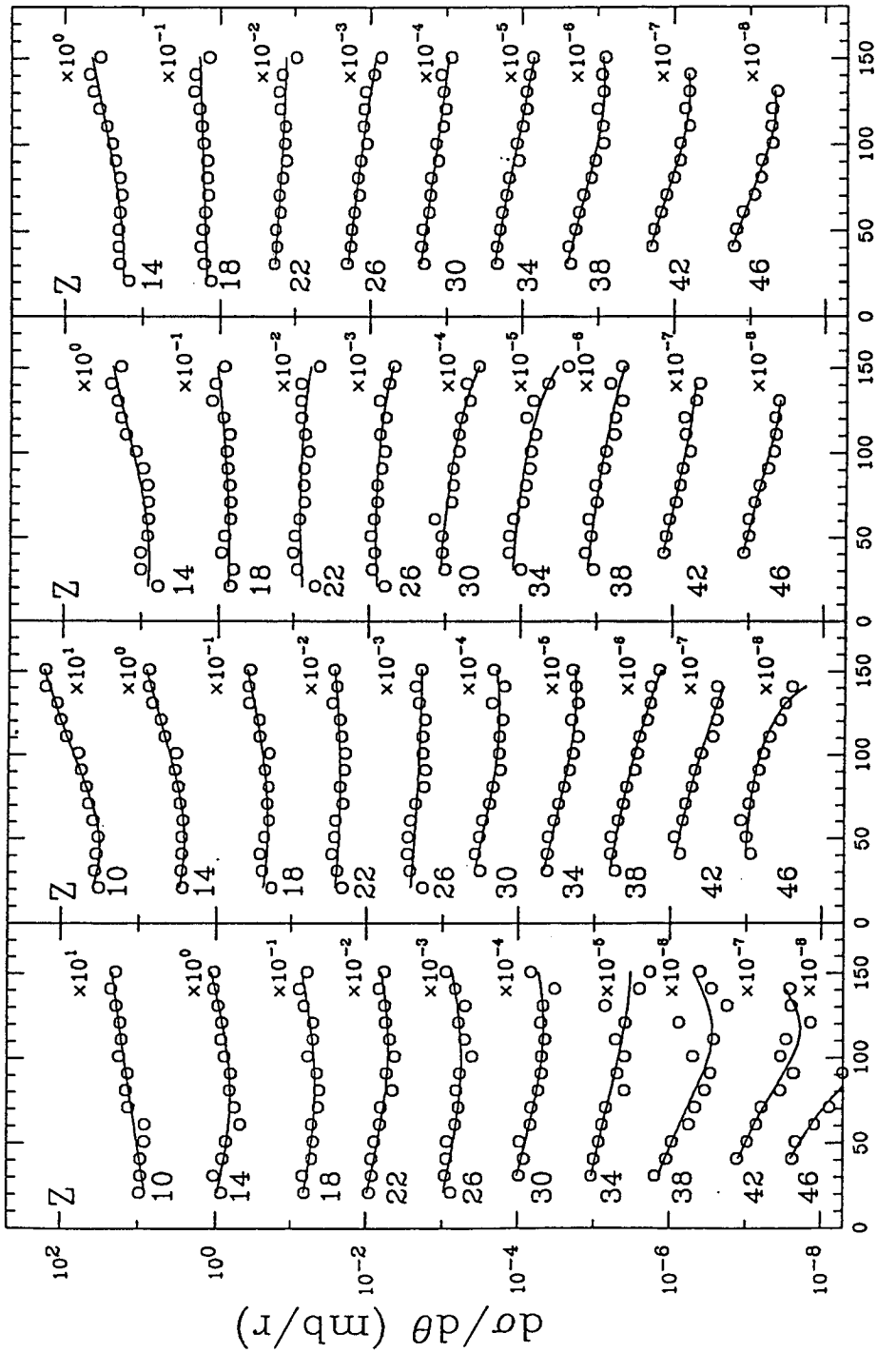

XBL 921-173

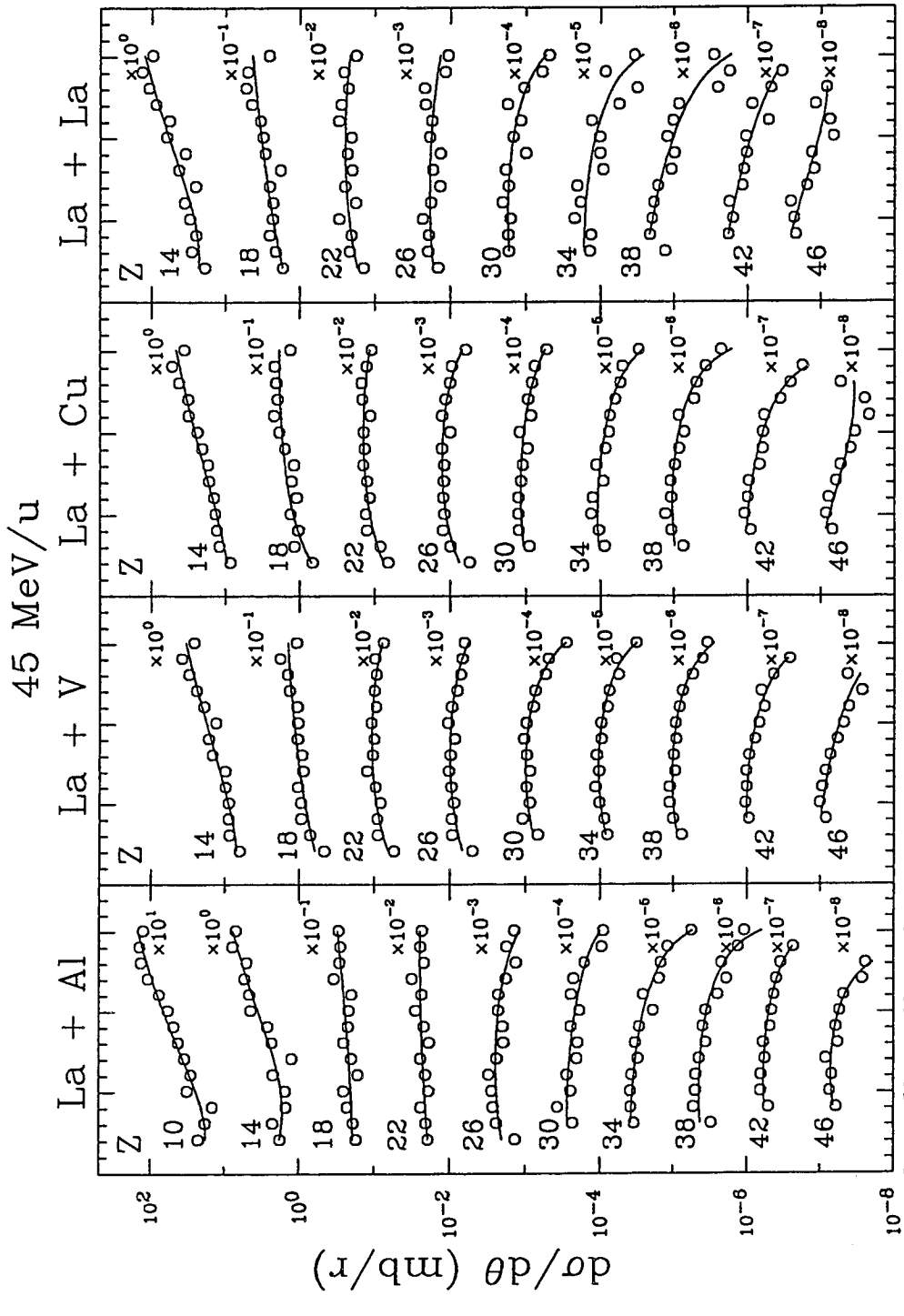

XBL 921-172

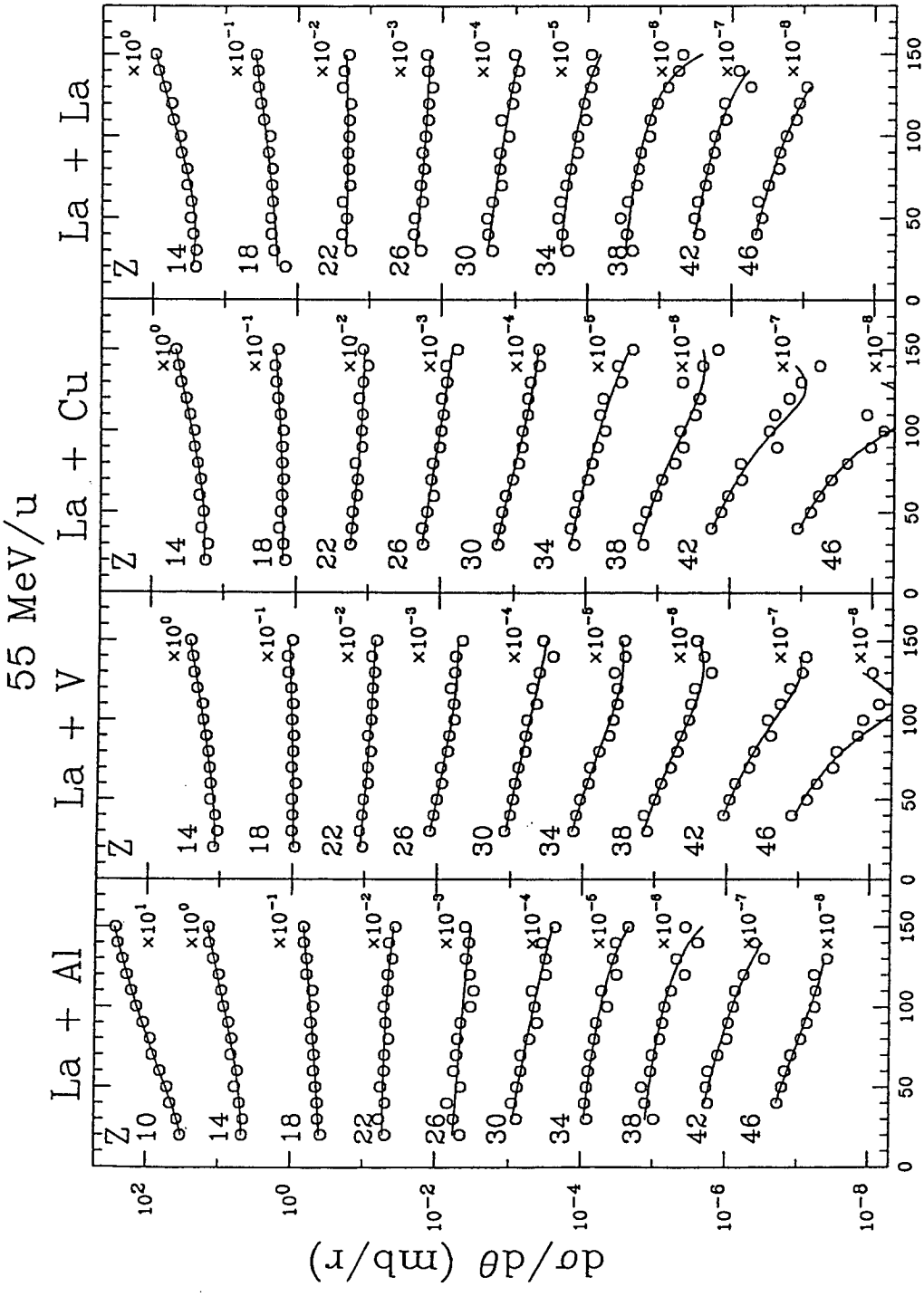

XBL 921-171

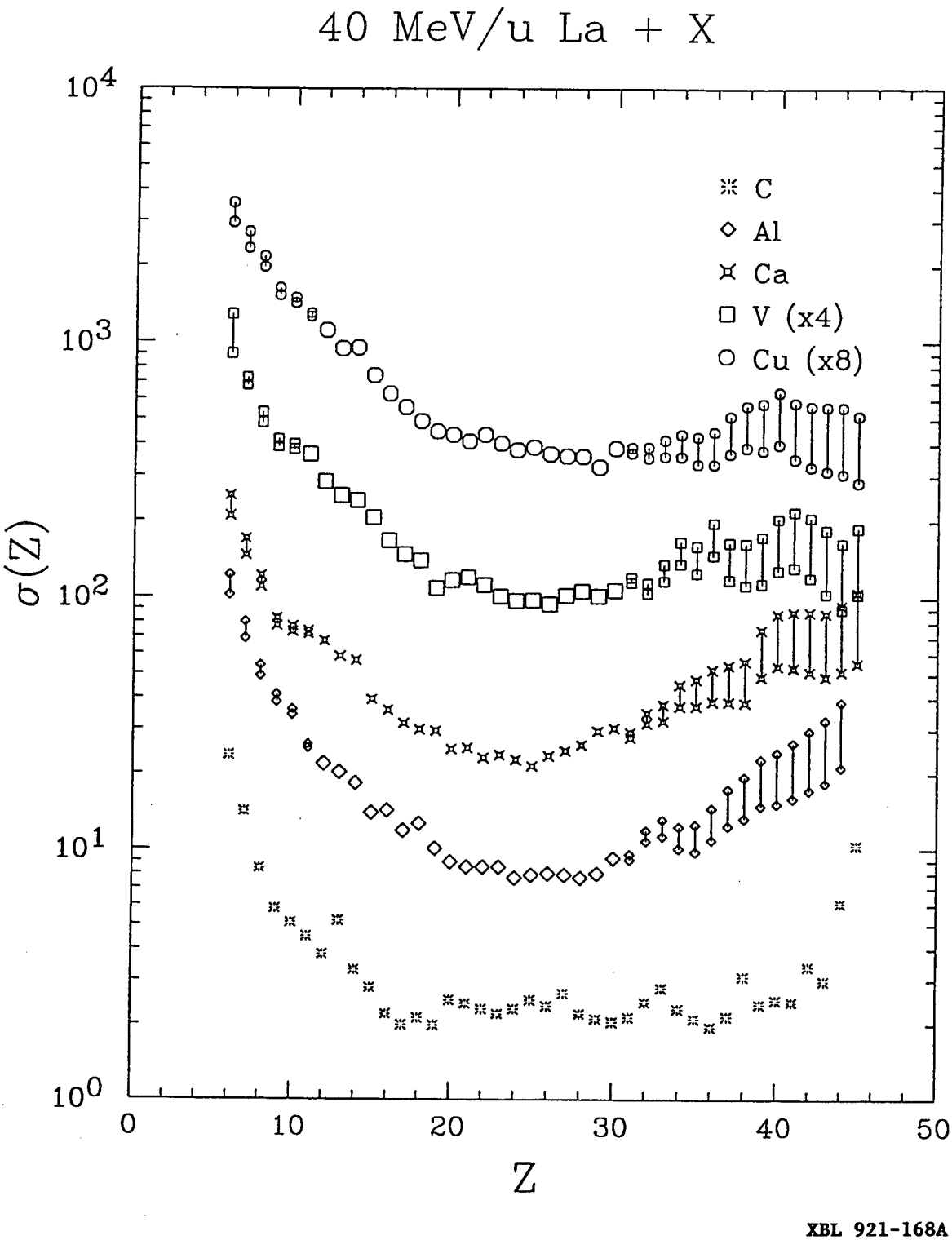
40 MeV/u La + X
10^4
10^3
10^2
10^1
10^0
σ(Z)
0
10
20
30
40
50
Z
C
Al
Ca
V (x4)
Cu (x8)

XBL 921-168A

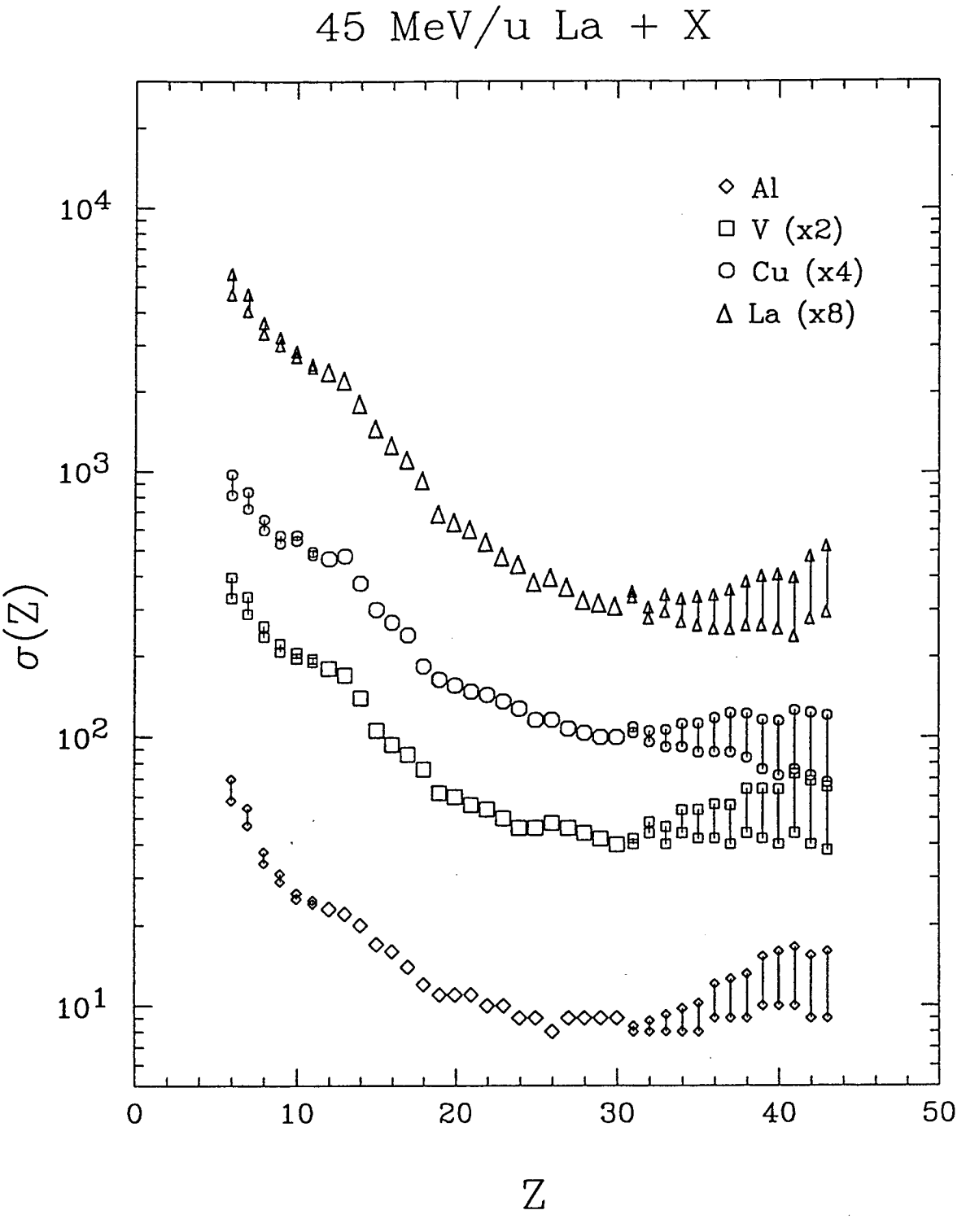

XBL 921-169A

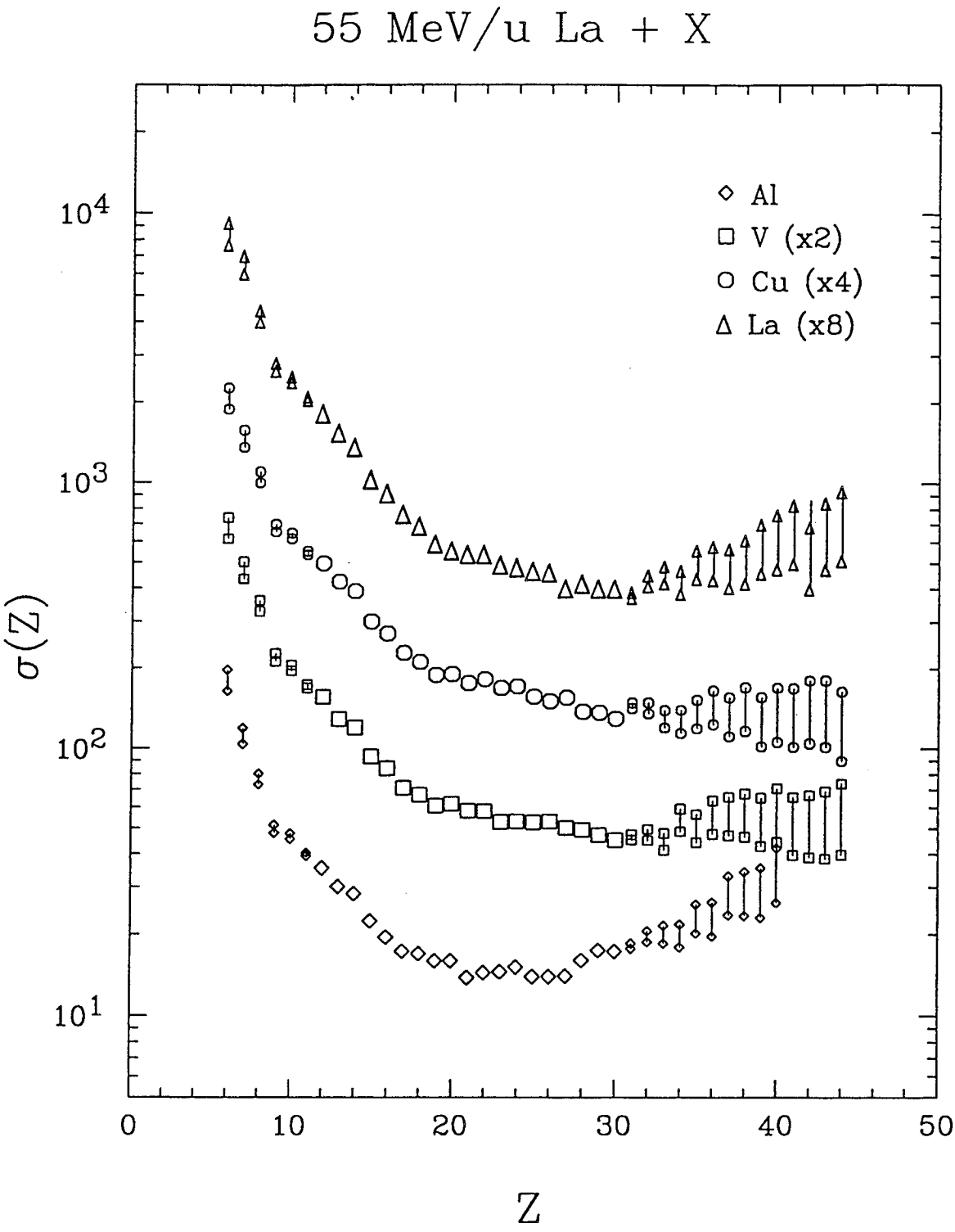

XBL 921-170A

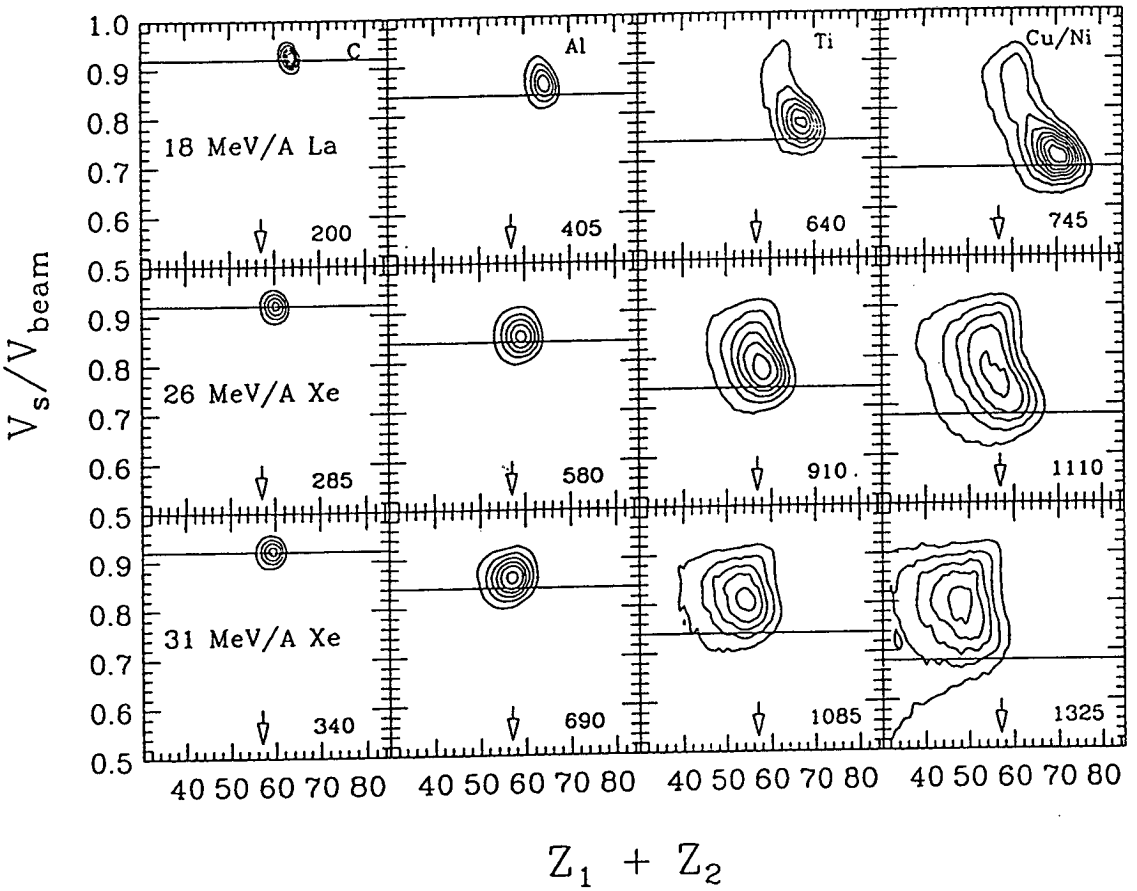
C
Al
Ti
Cu/Ni
18 MeV/A La
26 MeV/A Xe
31 MeV/A Xe
200
405
640
745
285
580
910
1110
340
690
1085
1325
1.0
0.9
0.8
0.7
0.6
0.5
40 50 60 70 80
V_s/V_{beam}
$Z_1 + Z_2$

XBL 921-164

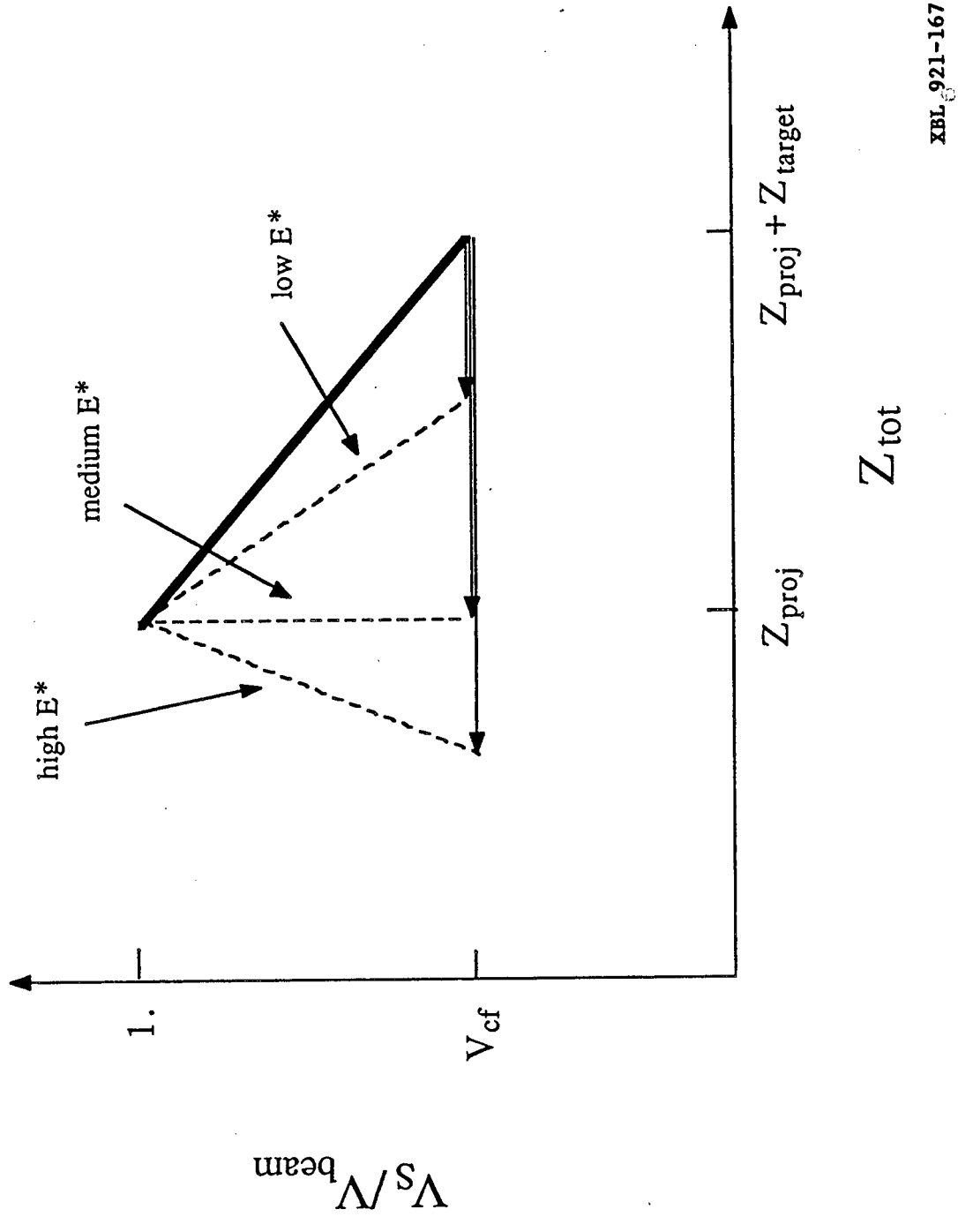

XBL 921-167

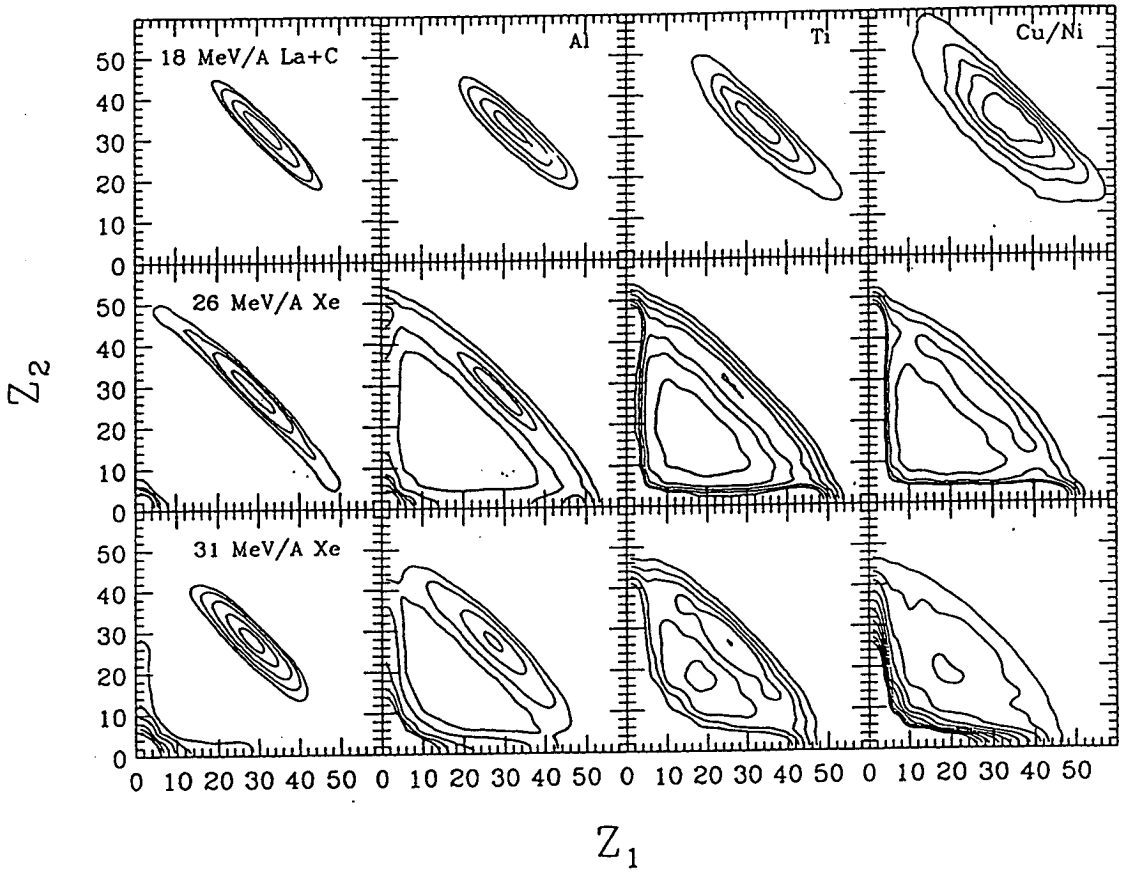

XBL 921-166

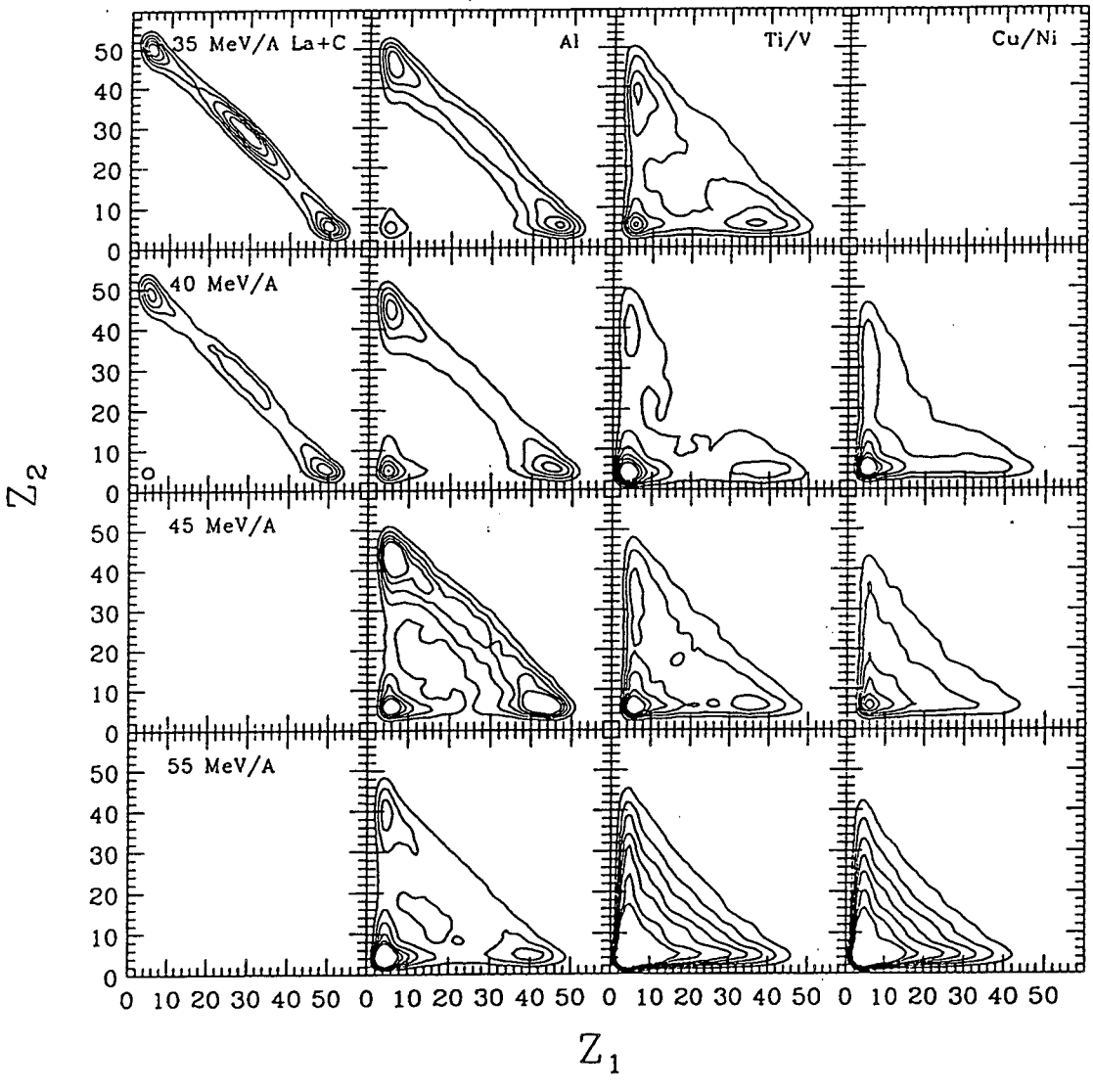
35 MeV/A La+C
Al
Ti/V
Cu/Ni
40 MeV/A
45 MeV/A
55 MeV/A
Z_2
Z_1
0 10 20 30 40 50

XBL 921-165

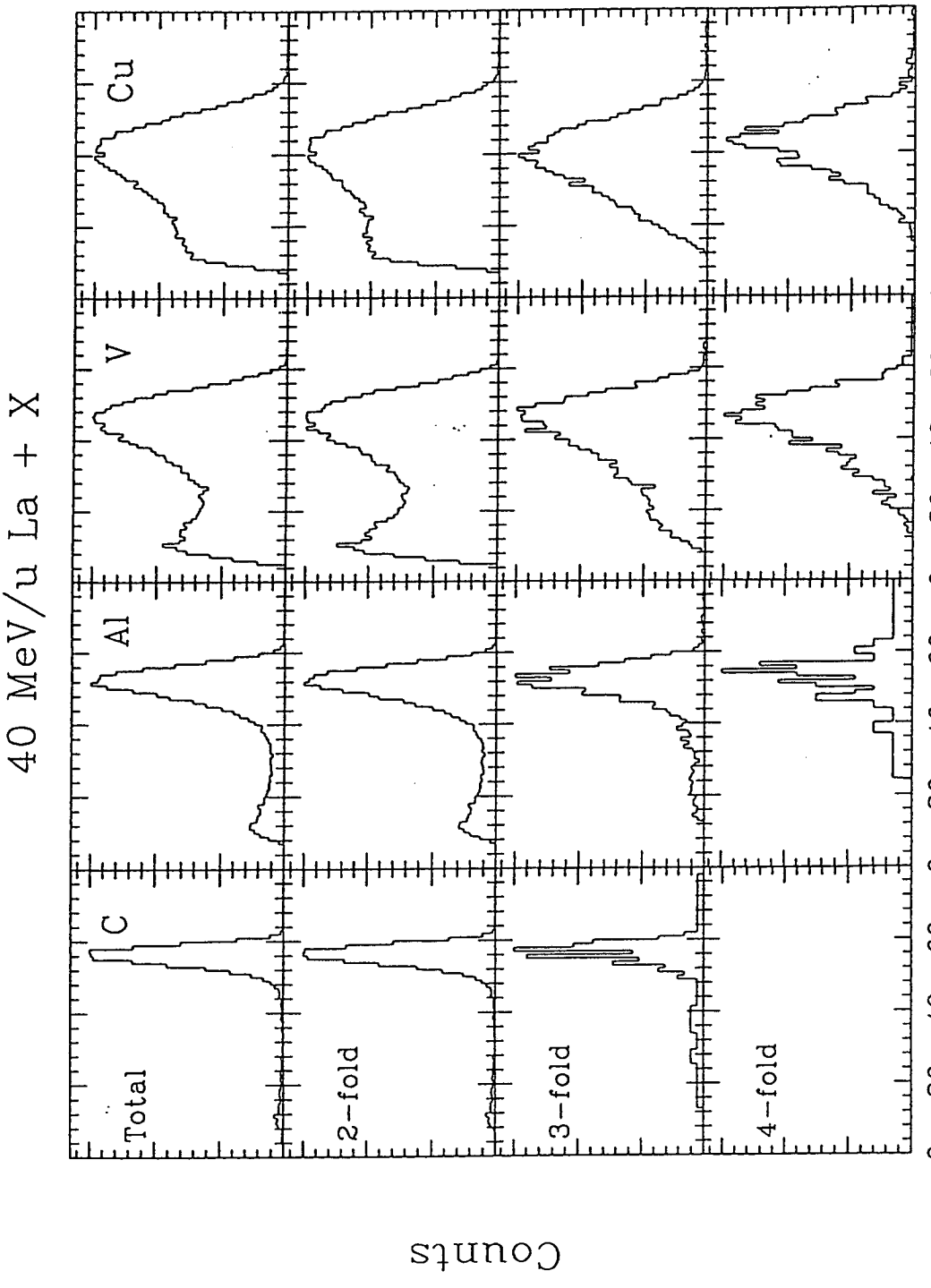
40 MeV/u La + X
C
Al
V
Cu
Total
2-fold
3-fold
4-fold
0
20
40
60
Counts
Z_{total}

XBL 921-162

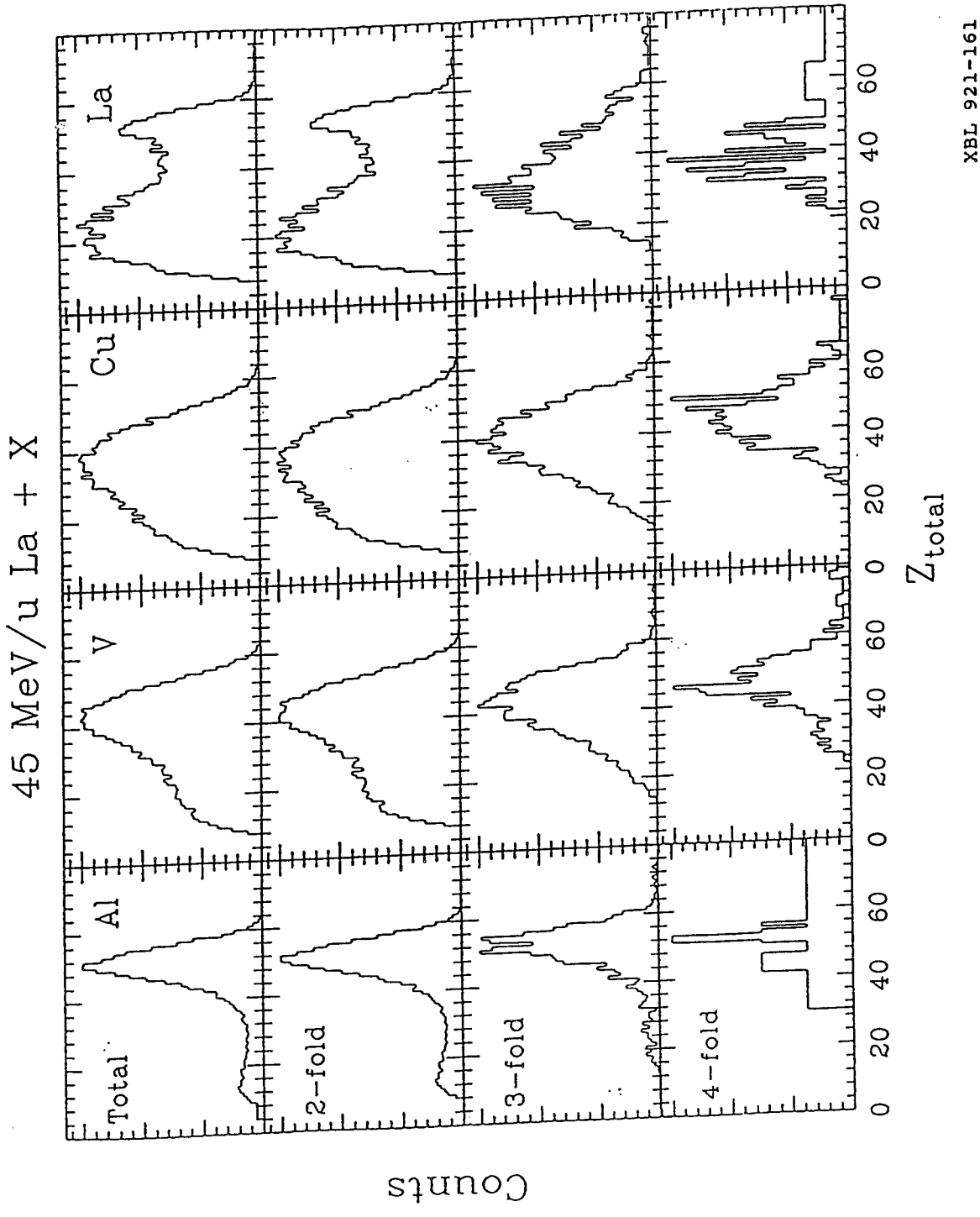
45 MeV/u La + X
Counts
Total
2-fold
3-fold
4-fold
Al
V
Cu
La
0
20
40
60
Z_{total}

XBL 921-161

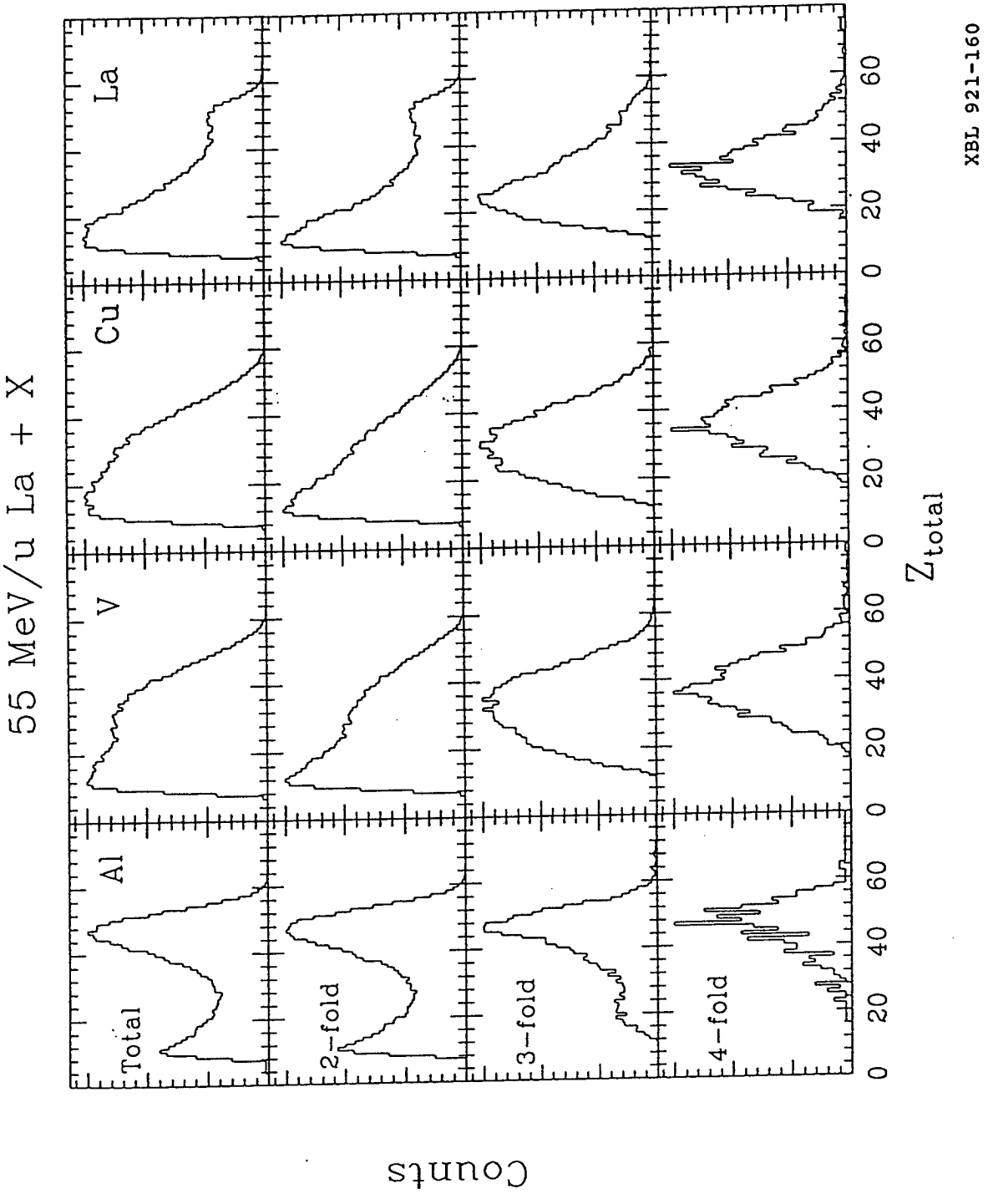
55 MeV/u La + X
Al
V
Cu
La
Total
2-fold
3-fold
4-fold
Counts
Z_{total}
0
20
40
60
XBL 921-160

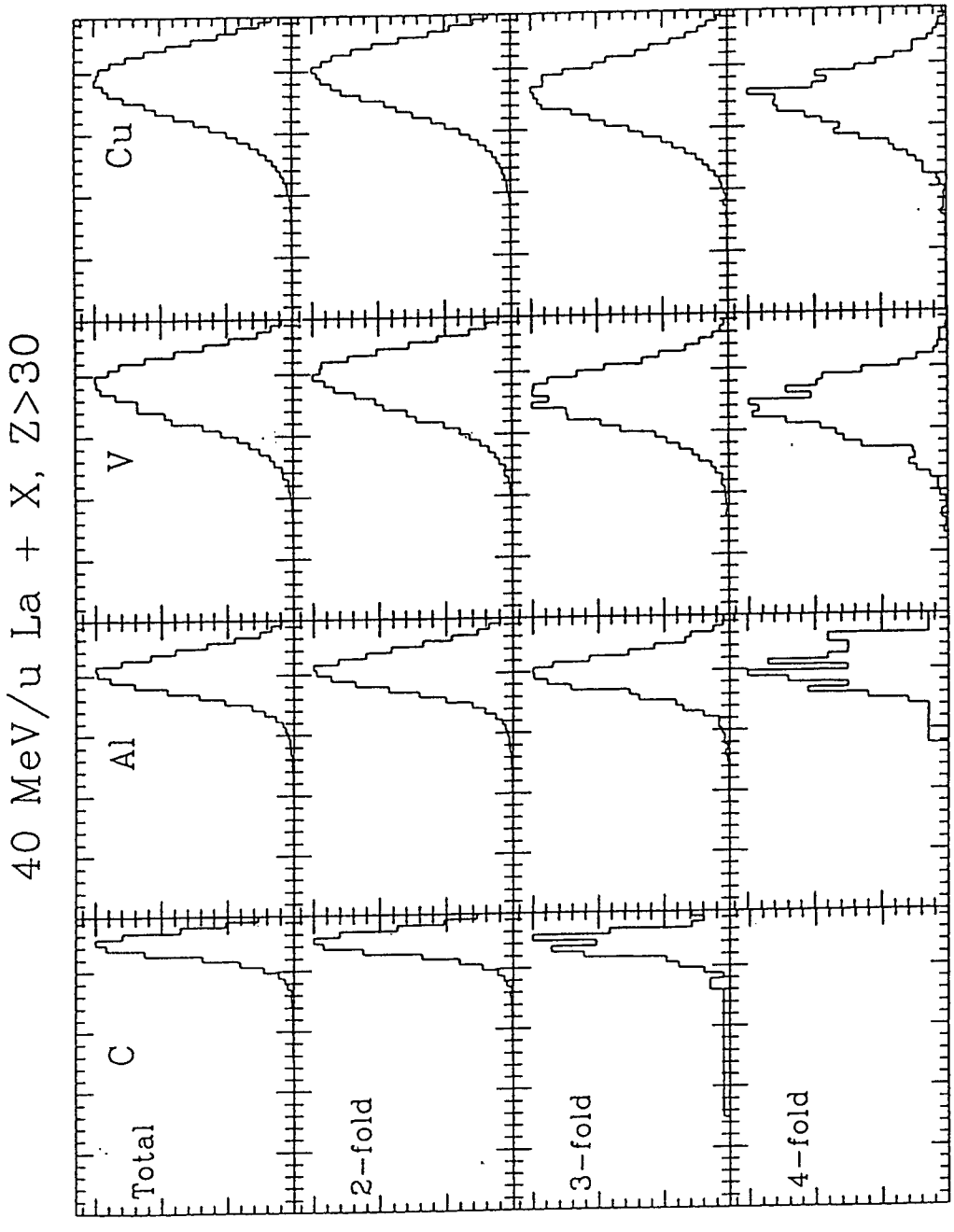
40 MeV/u La + X, Z>30
Counts
Total
2-fold
3-fold
4-fold
C
Al
V
Cu
0.5 0.6 0.7 0.8 0.9 0.5 0.6 0.7 0.8 0.9 0.5 0.6 0.7 0.8 0.9 0.5 0.6 0.7 0.8 0.9
V_S/V_{beam}

XBL 921-159

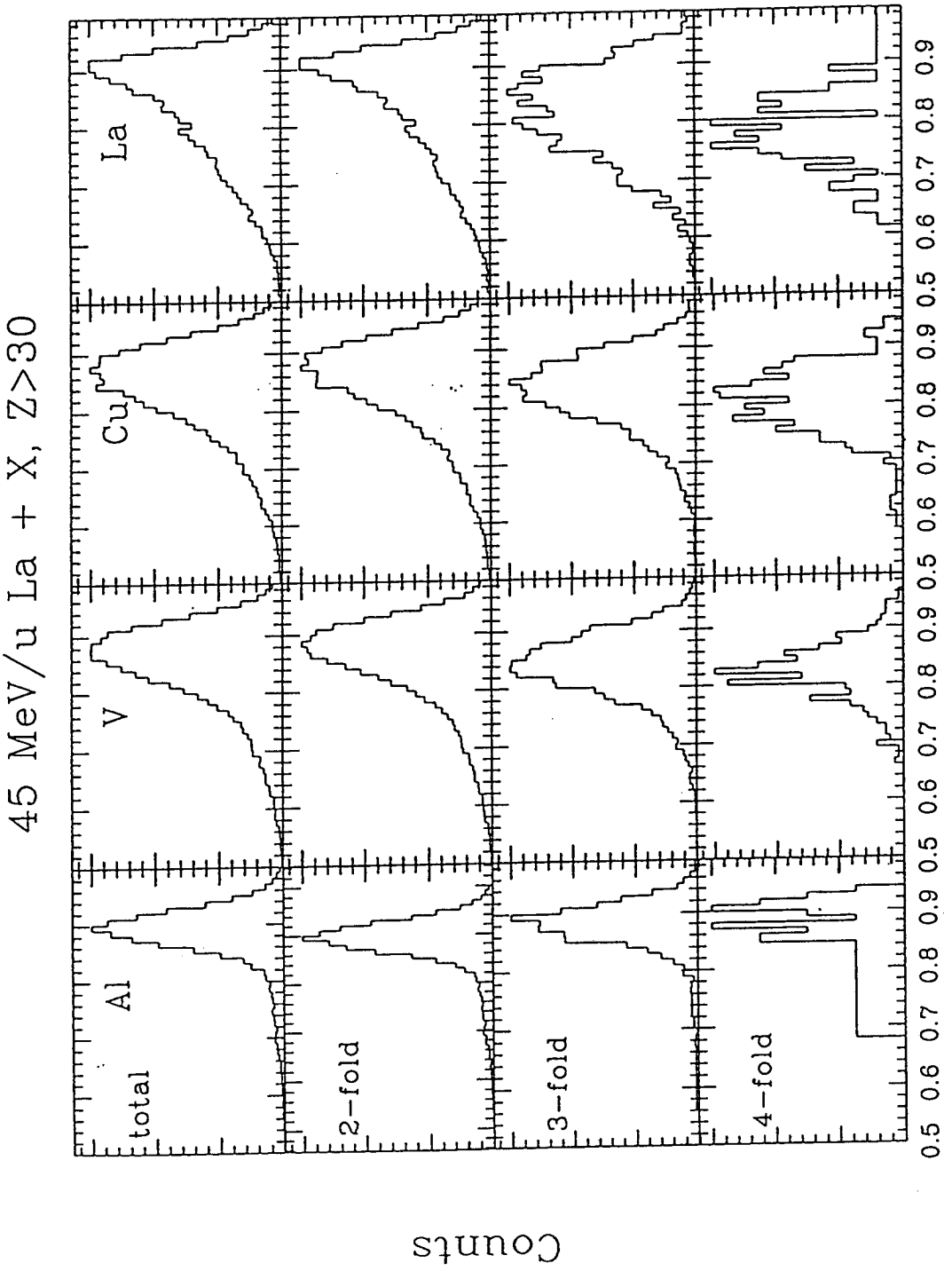
45 MeV/u La + X, Z>30
Counts
total
2-fold
3-fold
4-fold
Al
V
Cu
La
0.5 0.6 0.7 0.8 0.9 0.5 0.6 0.7 0.8 0.9 0.5 0.6 0.7 0.8 0.9 0.5 0.6 0.7 0.8 0.9
V_s/V_{beam}
XBL 921-158

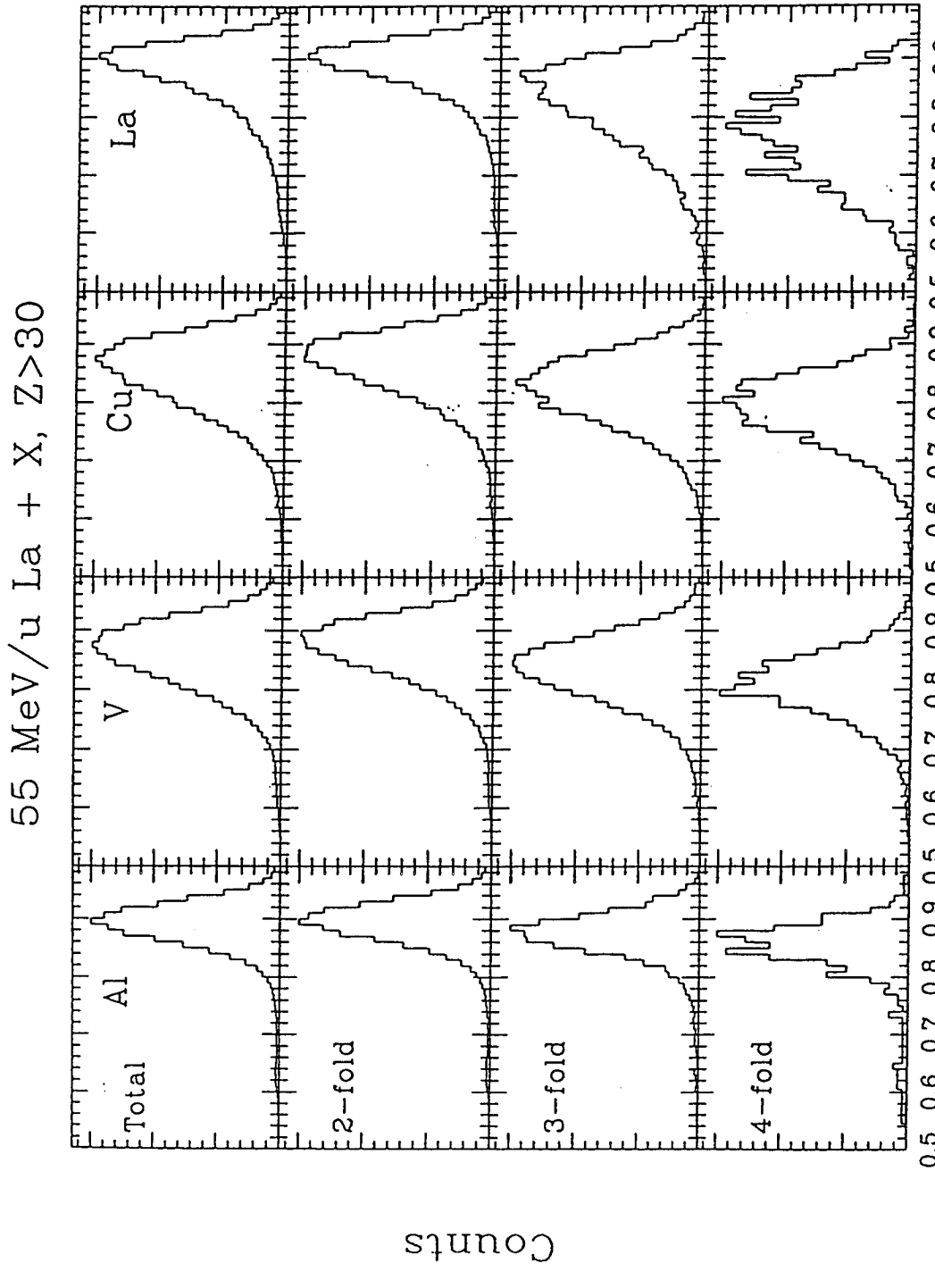
55 MeV/u La + X, Z>30
Counts
Total
2-fold
3-fold
4-fold
Al
V
Cu
La
0.5 0.6 0.7 0.8 0.9
V_S/V_{beam}

XBL 921-157

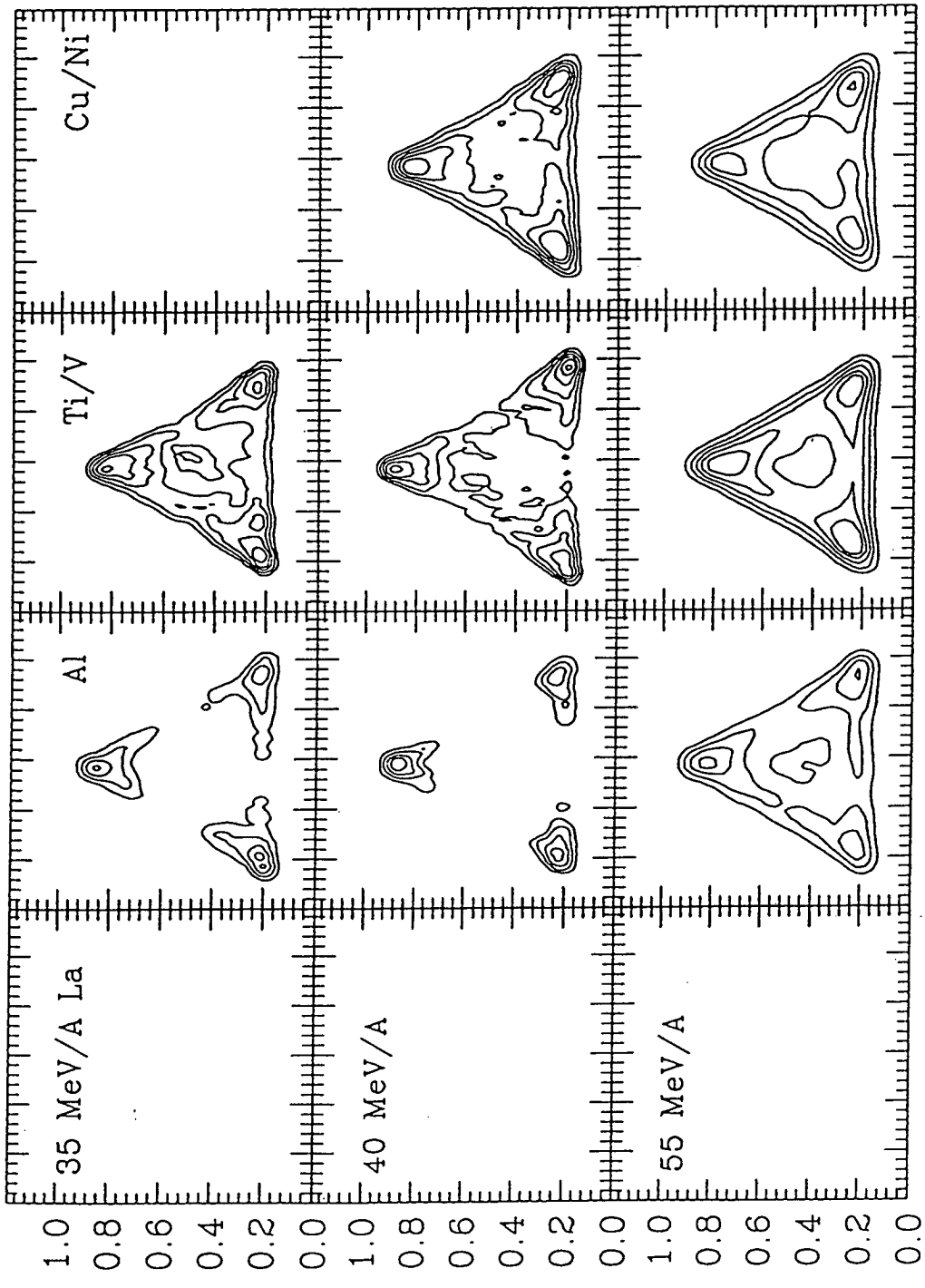
35 MeV/A La
40 MeV/A
55 MeV/A
Al
Ti/V
Cu/Ni
0.0
0.2
0.4
0.6
0.8
1.0
0 .2 .4 .6 .8 1. 0 .2 .4 .6 .8 1. 0 .2 .4 .6 .8 1.

XBL 921-156

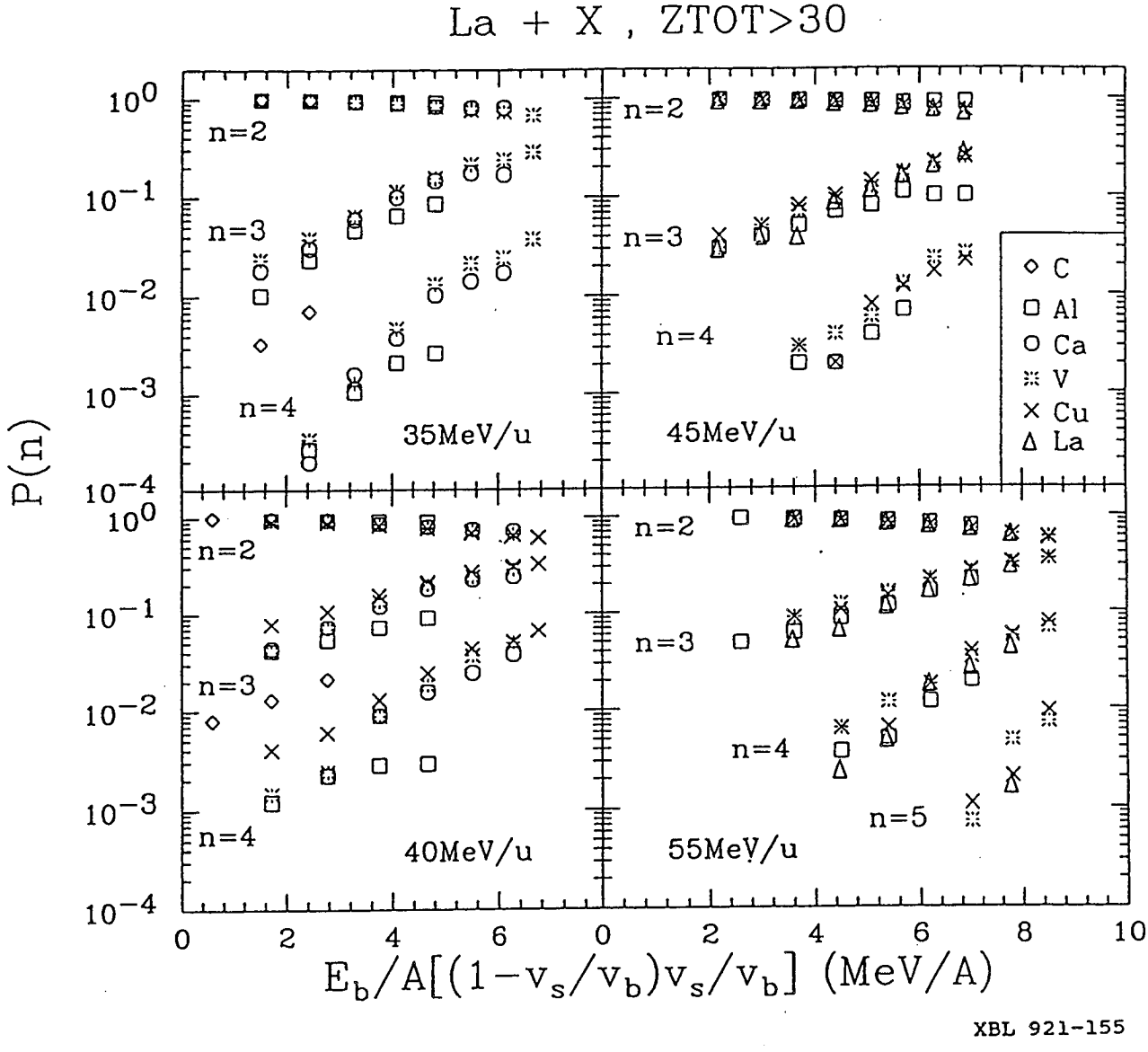
La + X , ZTOT>30
P(n)
10^0
10^{-1}
10^{-2}
10^{-3}
10^{-4}
n=2
n=3
n=4
n=5
35MeV/u
45MeV/u
40MeV/u
55MeV/u
C
Al
Ca
V
Cu
La
0
2
4
6
8
10
$E_b/A[(1-v_s/v_b)v_s/v_b]$ (MeV/A)
XBL 921-155

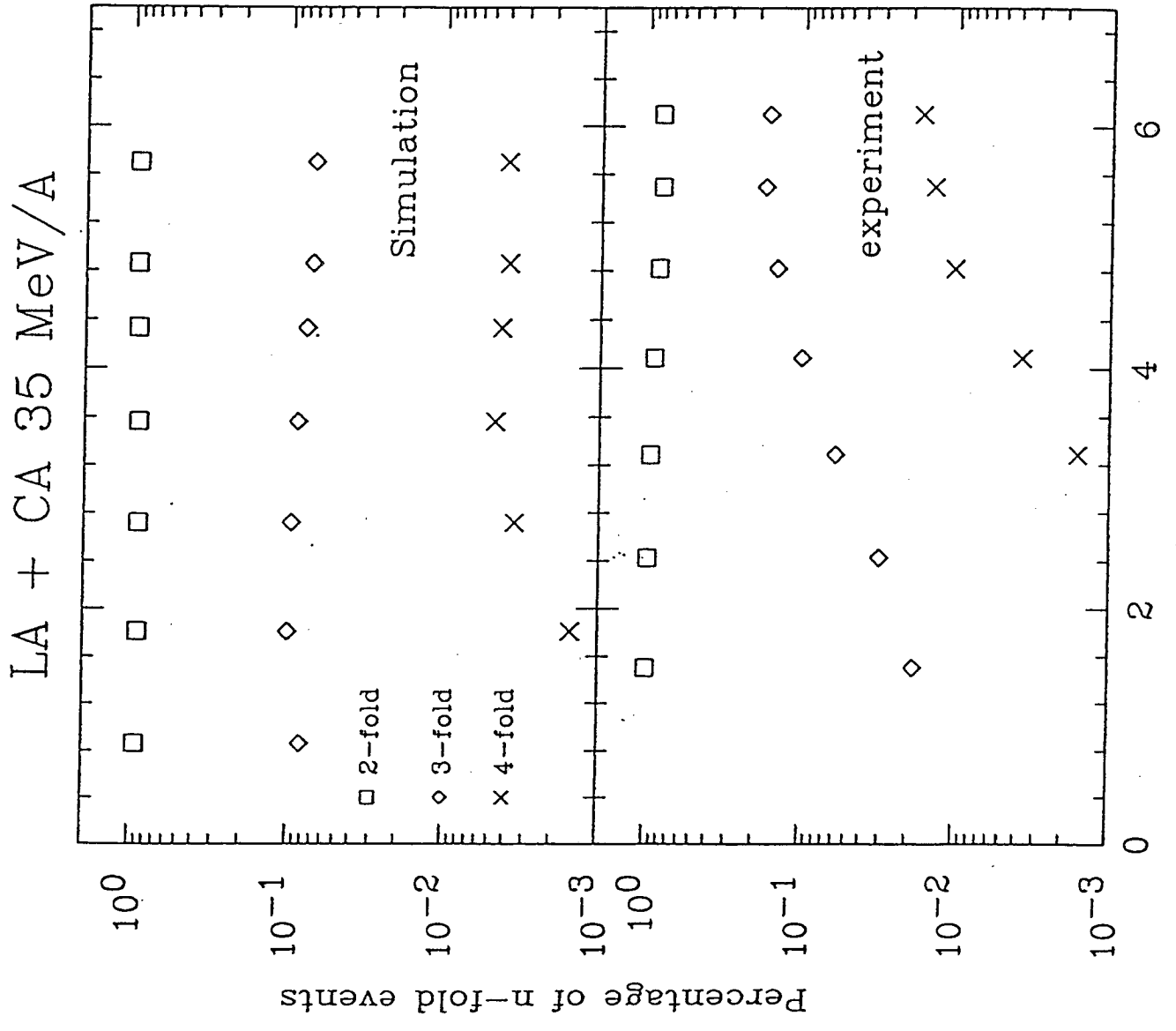
LA + CA 35 MeV/A
Simulation
experiment
□ 2-fold
◇ 3-fold
× 4-fold
Percentage of n-fold events
E/A (MeV/A)
10^0
10^-1
10^-2
10^-3
0
2
4
6

LAWRENCE BERKELEY LABORATORY
UNIVERSITY OF CALIFORNIA
TECHNICAL INFORMATION DEPARTMENT
BERKELEY, CALIFORNIA 94720